TITLE:
Multi-stage-mixing to create a core-then-shell structure improves DNA-loaded lipid nanoparticles' transfection by orders of magnitude

AUTHORS:
Jia Nong[1]*, Xijing Gong[2,3]*, Quang Minh Dang[1,2,3], Sachchidanand Tiwari[3,4], Manthan Patel[1,3], Jichuan Wu[3], Andrew Hanna[2], Wook-Jin Park[5], Elena N. Atochina-Vasserman[5], Hui-Ting Huang[6], Oscar A. Marcos-Contreras[1], Kahlilia C. Morris-Blanco[6], Jonathan J. Miner[7], Drew Weissman[5], Vladimir R. Muzykantov[1], Kushol Gupta[8], David Issadore[2], Jacob W. Myerson[1,2], Zhicheng Wang[1,3#], Jacob S. Brenner[1,2,3#]

[1]Department of Systems Pharmacology and Translational Therapeutics, Perelman School of Medicine, University of Pennsylvania, Philadelphia, PA, USA.
[2]Department of Bioengineering, University of Pennsylvania, Philadelphia, PA, USA
[3]Division of Pulmonary, Allergy, and Critical Care, Department of Medicine, Perelman School of Medicine University of Pennsylvania, Philadelphia, PA, USA
[4]Department of Microbiology, Perelman School of Medicine, University of Pennsylvania, Philadelphia, PA, USA
[5]Division of Infectious Diseases, Perelman School of Medicine, University of Pennsylvania, Philadelphia, PA, USA
[6]Department of Cell & Developmental Biology, Perelman School of Medicine, University of Pennsylvania, Philadelphia, PA, USA
[7]Division of Rheumatology, Department of Medicine, Perelman School of Medicine, University of Pennsylvania, Philadelphia, PA, USA
[8]Department of Biochemistry & Biophysics, Perelman School of Medicine, University of Pennsylvania, Philadelphia, PA, USA

*equal contribution
#co-corresponding authors

ABSTRACT:
The unprecedented success of mRNA-lipid nanoparticles (LNPs) has highlighted their power for protein expression, but the hours-long half-life of mRNA severely limits their use in chronic diseases. In contrast, DNA LNPs display months-long expression and genetically encode cell type specificity, but their use has been hindered by poor protein expression (orders of magnitude lower than mRNA LNPs). To overcome this, we introduce multi-stage mixing (MSM) microfluidics to control the internal structure of LNPs and use it to create core-then-shell (CTS) structured DNA LNPs. CTS LNPs display distinct thermal transitions and internal organization compared to the amorphous structure of conventional LNPs. CTS improves transfection by three orders of magnitude *in vitro*, outperforming gold standard reagents in hard-to-transfect cells like primary neurons. *In vivo*, CTS DNA LNPs augment expression by two orders of magnitude, achieving peak expression levels comparable to mRNA LNPs, but with prolonged expression. This work demonstrates how microfluidic control over nanoparticle assembly kinetics can access otherwise unattainable particle architectures, advancing both materials science and therapeutic applications.

INTRODUCTION:
The billion-patient success of the COVID-19 mRNA lipid nanoparticle (LNP) vaccine demonstrated the unparalleled ability of LNPs to drive expression of chosen proteins [1]. This has led to >>$10B investment by industry and governmental funders in developing LNPs therapeutics, nearly all of focused on mRNA cargo. However, mRNA has two fundamental

limitations: i) a half-life of hours, which precludes treatment of chronic diseases [2]; ii) no promoter region, so an inability to control cell-type-specific protein expression, shifting most LNP-stimulated protein expression to leading to off-target cell types [3].

DNA can solve both problems, as it has intrinsic intracellular stability for years and has promoters which can drive exquisite cell-type-specificity. Unfortunately, in the 20 years of LNP development, DNA-loaded LNPs (DNA LNPs) were never advanced because they suffered from two different problems: a) DNA LNPs were found to be very toxic, killing naive mice within 2 days at moderate doses; b) DNA LNPs induce protein expression at levels many orders of magnitude less than that of mRNA LNPs. We recently solved the first problem [4]. We began by showing that the toxicity of DNA LNPs is caused by detection of cytosolic DNA by the cGAS-STING pathway, which then activates massive inflammation. Next, we loaded DNA LNPs with nitrated lipids, which are mammals' natural negative feedback inhibitor of STING. DNA LNPs loaded with such STING-inhibiting lipids (e.g., nitro-oleic acid) eliminated DNA LNP mortality. Further, these STING-inhibiting DNA LNPs stably express protein *in vivo* for at least 3 months per dose.

However, STING inhibition alone was not sufficient to fix the second problem of DNA LNPs, that they have protein expression levels 1,000- to 10,000-fold lower than the peak of mRNA LNP expression. Here we set out to solve that problem. There are five major hurdles that DNA LNPs face for achieving protein expression (**Fig. 1A**): 1) LNP synthesis has been optimized for mRNA, not DNA, and this may lead to deleterious alterations to DNA's structure [5, 6]. Next, after the LNPs are delivered to cells and the LNPs achieve endosomal escape, DNA cargo face intracellular hurdles: 2) Intracellular DNA sensors, such as cGAS-STING and AIM2, repress protein translation upon sensing cytosolic DNA [7]; 3) Intracellular DNases rapidly degrade DNA if it is found outside the nucleus [8] ; 4) slow cytosolic trafficking of DNA towards the nucleus in viscous cytoplasm [8]; and 5) nuclear entry of pDNA is highly inefficient, in large part because the nuclear pore complex does not permit cargo > 39 nm [9].

To overcome all five hurdles at once, here we have reimagined the LNP synthesis process, with one initial goal: *compactify* the DNA. If we could pack the DNA into a "core" at the start of LNP synthesis in the optimal buffer (problem #1), it would provide a physical barrier to intracellular DNA sensors (#2) or DNases (#3), and it would increase the mobility of plasmid DNA in the cytoplasm (#4) and fit more easily through the nuclear pore complex (#5). To accomplish the compact packaging of DNA inside LNPs, here we innovated the first practical multi-stage mixing (MSM) LNP synthesis. In standard LNPs, there is a single mixing step: the nucleic acid (in aqueous buffer) is mixed with the lipids (in organic solvent) via microfluidics or confined impingement jet mixing (**Fig. 1C**). In MSM production of core-then-shell (CTS)-DNA LNPs, there are two stages of mixing (**Fig. 2A**). First, DNA is mixed with the cationic lipid DOTAP and the zwitterionic lipid DOPE to form a "core". Prior research shows that certain ratios of DNA, DOTAP and DOPE can form lipoplexes containing inverse hexagonal phase, a lipid structural motif known to enhance endosomal escape by LNPs [10, 11]. In addition, compactifying DNA at an N:P ratio of less than 2 is reported to form relatively loose complex and enhance nuclear delivery efficiency, while a high N:P ratio would result in tightly-condensed rigid-body-like particles. Since the nuclear pore complex can only facilitate a < 39 nm rigid body passing through, condensing DNA too tightly within nanoparticles might impose a negative effect on the nuclear entry [12]. Thus, here we kept the ratio of DOTAP low to avoid forming rigid bodies of tens of nanometer in diameter, and achieve instead loose condensation of DNA. However, these lipoplex cores are not thermodynamically stable, aggregating to >2000nm, making them unfeasible for loading into LNPs or injecting *in vivo*. The MSM approach encapsulates these lipoplexes in a lipid in the standard LNP lipids before they have a chance to grow, forming a shell around the core and rescuing their stability and feasibility for *in vivo* delivery.

Using a variety of physical characterization methods, we show that MSM produces DNA LNPs with a radically different structure than standard LNPs, with the structure matching the hypothesized core and shell. Further, we show that CTS LNP structure improves *in vitro* DNA transfection by several orders of magnitude, even in classically "hard-to-transfect" primary cells like cortical neurons and mouse embryonic fibroblasts. Finally, we show that co-loading CTS DNA LNPs with the STING inhibitor C-178 improves expression further, even beating the decades-old gold standard of Lipofectamine in *vitro*, and drives *in vivo* protein expression at levels that are multiple orders of magnitude higher than standard DNA LNPs, and now comparable to mRNA LNPs at their peak.

RESULTS:

Optimizing the buffer used during LNPs synthesis improves DNA stability, and markedly improves DNA-based protein expression

The first hurdle in DNA LNPs reaching maximal expression is that the standard synthesis conditions of LNPs may alter DNA's structure in deleterious ways. In mRNA LNP synthesis, the nucleic acid is dissolved in a pH 4 buffer (typically citrate) to maximize protonation of ionizable lipids and improve ionic interactions between the mRNA and the ionizable lipids [13]. However, this low pH may destabilize the helix and lower the thermal melting point of DNA, and cause DNA to adopt conformations other than the classical right-handed double helix B form, the most common biologically active structure present in cells under normal physiological conditions. Other conformations can include A-form, Z-form, G-quadruplex, and others, as well as less defined conformations that might occur after partial acid hydrolysis of the DNA [14].

To assess the effect of buffer and pH on DNA conformations, we analyzed plasmid DNA (pDNA) in different buffers by circular dichroism (CD) spectroscopy, which measures B-form DNA via relative magnitude of the ellipticity signal in the range of 200 - 320 nm. A typical B-form DNA has a positive maximum around 290 nm, a negative maximum around 245 nm and a broad positive peak between 260 - 280 nm. We compared two different buffers: pH 4 citrate (classic mRNA LNP synthesis buffer) vs pH 6 TBS with 4 mM Mg^{2+}. Tris is the most common buffer used in DNA reactions, and Mg^{2+} stabilizes the B-form DNA helix via a variety of mechanisms, mostly involving electrostatic interaction between Mg^{2+} and DNA's phosphates [15]. As shown in **Fig. 1B**, the CD spectroscopic signal for B-form DNA signal is significantly disrupted by citrate buffer vs TBS buffer. Titrating Mg^{2+} in the TBS buffer, we found that 4 mM Mg^{2+} slightly improves B-form DNA signal in CD spectroscopy, compared to 0 and 12.5 mM Mg^{2+} (**Supplementary Fig 1A**). These results suggest that the traditional buffer used during LNP synthesis (pH 4 citrate without Mg^{2+}) perturbs the DNA B-form conformation, and this defect can be rescued by switching to pH 6 TBS buffer containing 4 mM Mg^{2+}.

Having shown that buffer choice can affect the DNA conformation, we next determined if the buffer choice similarly affects DNA LNPs' ability to drive protein expression. We synthesized DNA LNPs using a standard LNP formulation and encapsulating pDNA encoding luciferase (**Fig. 1C**). We synthesized LNPs in one of two buffers, pH 4 citrate or pH 6 TAE, which is another Tris-based buffer containing EDTA. After synthesis, we performed the standard dialysis on LNPs. Instead of using solely the standard phosphate buffer saline (PBS), we compared the PBS dialysis buffer with and without Mg^{2+}. The structure of the buffer-optimized LNPs was analyzed by cryo-electron microscopy (CryoEM, **Fig. D**). We found that the optimal DNA LNPs (TBS, pH 6, Mg^{2+}) had similar morphology to standard LNPs (citrate, pH 4, no Mg^{2+}).

In *in vitro* transfection experiments, RAW 264.7 macrophages were treated with these DNA LNPs and luciferase expression was measured at 24 and 48 hours (**Fig. 1E-F**). The Tris-based buffer led to greater expression than the citrate buffer, fitting with Tris buffer preserving B-form DNA (**Fig. 1B**). Mg^{2+} in the dialysis buffer was essential for any expression at all, again fitting with the importance of Mg^{2+} for stabilizing DNA structure. It is worth noting that the

addition of Mg^{2+} in acidic buffer did not have positive effects on (**Supplementary Fig. 1B**), possibly due to weakened Mg^{2+}-DNA interactions in proton-rich acidic buffer. Additionally, Mg^{2+} can act as a cofactor of DNA related enzymes such as DNase I and topoisomerase [16].

Next, we compared a broader range of synthesis buffers for their ability to produce DNA LNPs that drive high level of protein expression in RAW macrophages (**Fig. 1G-I**). Luciferase expression by TBS vs. TAE and HEPES, with pH 6 being better than pH 5. Addition of Mg^{2+} in TBS further improves performance. We also confirmed this general trend in a second cell line, HeLa epithelial cells (**Fig. 1J-L**), except that TAE outperforms TBS when Mg^{2+} is present. These results confirm that across multiple cell types, Tris buffers at pH 6 are best, and Mg^{2+} is essential for enhanced DNA expression.

Multi-stage mixing (MSM) to create core-then-shell (CTS) LNPs improves the encapsulation of nucleic acids

While buffer optimization preserves DNA stability during LNP synthesis, that is only the first hurdle DNA LNPs face compared to mRNA LNPs (**Fig. 1A**). Buffer optimization only improves luciferase expression to ~10% of that achieved by Lipofectamine, the gold-standard *in vitro* transfection reagent (**Fig.1G-L**). The remaining hurdles prevent effective DNA expression. These hurdles could be solved individually by various *chemical* and *genetic* methods, such as covalent modification of DNA, co-loading inhibitors, and helper RNA molecules. However, a more elegant approach would attack all intracellular hurdles without requiring the risks of introducing new chemical and genetic entities. To do this, we sought a *physical* method that would solely change how we pack DNA into LNPs. We aimed to compactly package DNA into a "core," which might protect DNA from DNA sensors and DNases, and hold DNA in a complex that can more easily fit through the nuclear pore complex.

To produce LNPs with a "core" of DNA, we developed multi-stage mixing (MSM) LNP synthesis (**Fig. 2A-B**). In Mixing Stage 1, DNA (here plasmid DNA) is mixed with the zwitterionic lipid DOPE and a cationic lipid DOTAP to form a "core". These cores are immediately mixed with the standard LNP lipids, which form a "shell" around the core. Thus, we call these "core-then-shell" (CTS) DNA LNPs.

Based on lipoplex studies showing that an N:P of DOTAP:DNA ratios above 2 impede nuclear delivery of DNA, we selected a DOTAP:DNA N:P of 0.63 [12]. Notably, this leaves DOTAP at a final molar % of total lipids of only 1.96%. This is far below the 10-50% range used for DOTAP LNPs with lung tropism, which we previously showed induced thrombosis [17, 18]. Indeed, we show in **Supplementary Fig. 2** that this low level of DOTAP does not induce accidental lung tropism or clotting.

This initial version of CTS produces LNPs that are bigger than standard DNA LNPs, but the polydispersity index (PDI) is also lower (**Fig. 2C**). The ζ-potential of the LNPs measured in *bulk* (a population measure) on a ZetaSizer shows that CTS LNPs are less negatively charged than standard DNA LNPs (made via standard two-channel mixing, shown in **Fig. 1C**), but the CTS LNPs are still -5 mV (**Fig. 2D**). This slight negative surface charge is important in the context of known toxicities of positively charged LNPs, which was theoretically possible here, given the presence of a small amount of a cationic DOTAP in the LNPs. Importantly, the DNA entrapment efficiency is ~90% for both standard (std) LNP and CTS LNP (**Fig. 2E**).

Next, we compared nucleic acid loading efficiency and uniformity for CTS LNPs made via MSM CTS vs. standard LNPs. We note multiple recent studies showing that within a standard LNP population, only a small fraction of the individual particles is actually loaded with detectable mRNA, while the rest are "empty" (undetectable mRNA) [19, 20]. We recently showed that empty LNPs are much more inflammatory than LNPs containing nucleic acids [21]. We loaded fluorescently labeled DNA, and traced individual LNP via nanoparticle tracking analysis (NTA) on a Malvern Panalytical NanoSight. The NanoSight can trace all nanoparticles via light scattering (**Fig. 2F**, right panel), and detect whether each LNP contains detectable DNA

via the fluorescent signal (**Fig. 2F**, left panel). Comparing standard LNPs (**Fig. 2G**) with CTS LNPs (**Fig. 2H**), it is evident that a higher fraction of CTS LNPs have detectable DNA in them. This is quantified in **Fig. 2I**, which shows that 83% of CTS LNPs have detectable DNA, while only 53% of standard LNPs do. We observed a similar trend in CTS LNPs loaded with mRNA (**Fig. 2J-M**). The quantification results show that more than 95% of CTS LNPs contain detectable mRNA, while only 5% of standard LNPs do. This loading fraction depends on the RNA/DNA detection threshold of the assay and is likely sensitive to lipid composition and cargo identity. However, this data shows that at least for some LNP formulations, CTS provides nucleic acid loading that is more uniform across the population of particles.

Structural analysis reveals that core-then-shell (CTS) DNA LNPs possess a true core and shell that is highly distinct from traditional LNPs

To directly show that the CTS protocol generates LNP structures that are distinct from standard LNPs, we characterized LNPs with Cryo-electron microscopy (Cryo-EM), single particle zeta potential measurements, differential scanning microcalorimetry, small angle X-ray scattering (SAXS), and multi angle light scattering (MALS).

Cryo-EM revealed a unique morphological structure in CTS formulations that differs from standard LNPs (**Fig. 3A**). Standard LNPs exhibited a characteristic structure without any signs of blebbing [22]. In contrast, CTS LNPs displayed a distinctive core-shell architecture, marked by a well-defined central region surrounded by two distinct outer shells. This observation suggests that the CTS protocol enables a unique assembly of LNP components, resulting in a specific spatial arrangement of the nucleic acid payload and lipid components.

The MSM method employed and the inclusion of a small amount of cationic DOTAP may explain the resulting CTS structure. To investigate this, we measured particle ζ-potentials at the single-molecule level using an NTA that performs microelectrophoresis. We compared two compositionally identical formulations of DNA LNPs containing 1.96% DOTAP, prepared using different mixing methods: one with MSM microfluidics, as described in **Fig. 2A**, and the other using traditional single-step microfluidic mixing (shown in **Fig. 1C**). The ζ-potential distribution for MSM LNPs showed a broad range of moderate to large potentials like that of standard LNPs without DOTAP, ranging from 0 to -50 mV (blue and black curves in **Fig. 3B**). However, the DOTAP formulation produced with single-step mixing had two sharp peaks, one at +5mV and one at -5mV. Thus, MSM produces particles with significantly different surface charge properties compared to single-step mixing. These findings indicate that physicochemical properties are influenced not only by lipid composition but also by the mixing protocol.

To further investigate the lipid organization and physical stability of CTS formulations, we performed a thermal analysis using differential scanning calorimetry (DSC) (**Fig. 3C**). This technique can identify phase transitions and structural ordering by measuring the energy required to heat samples, providing insights into molecular organization. Thermograms of standard LNPs displayed a single, broad, shallow exothermic peak centered around 80°C, suggesting a relatively amorphous structure with heterogeneous thermal transitions. In contrast, CTS LNPs yield two sharp, well-defined exothermic peaks: a major transition at approximately ~75°C and a minor transition at ~85°C. The presence of these distinct thermal transitions indicates that CTS LNPs possess a more ordered internal architecture with defined structural domains. The contrasting thermal profiles between the two formulations strongly suggest that the CTS protocol produces LNPs with a fundamentally different internal organization compared to the standard formulation method.

We next applied different modalities of light scattering to quantitate the size and mass of these particles in solution. Using dynamic light scattering (DLS), we observe that CTS particles are almost two-fold larger in hydrodynamic radius (R_h) in solution when compared to the standard LNP formulation, with a lower polydispersity index (PDI) (**Fig. 3D**). CTS particles had a determined R_h of 151 Å ± 2.3 (PDI = 0.14) compared to 80.2 Å ± 2.5 (PDI = 0.28) for the

standard formulation. Consistent with these differences in size, the particles had very different retention times and weight-average mass profiles (M_w), as determined by size-exclusion chromatography in-line with multiangle light scattering (SEC-MALS) (**Fig. 3E&F**). CTS particles had a M_w = 23.7 MDa ± 2.1% across the sizing peak, whereas standard particles were almost five-fold smaller in mass (M_w = 5.4 MDa ± 3.1%). Owing to the larger size of the CTS particles, we were also able to determine the radius of gyration (R_g) for the CTS particles (39.5 nm ± 5.5%).

We next employed synchrotron small-angle X-ray scattering (SAXS) to further investigate the size and shape, and to better interrogate the internal structure of these particles. We employed in-line size-exclusion chromatography to minimize and measure the possible effects of sample polydispersity in our analyses by performing singular value decomposition (SVD) analysis (see **Methods** and **Supplementary Figure 3**). In this approach, very different scattering profiles were obtained for the CTS and standard particles (**Fig. 3G**), including well-defined primary Bragg peaks at *q*-values between ~0.1-0.25 $Å^{-1}$, indicative of a highly ordered internal structure (**Fig. 3H&I**). In this experimental configuration (where $q_{min}*D_{max} \leq \pi$), it was possible to determine the size and shape of the standard LNP using the inverse Fourier transform (R_g of 156 Å, D_{max} of 400 Å), and to calculate *ab initio* electron density at low resolution (**Table 1** and **Supplementary Fig. 3**). It was not possible to apply the same conventional approaches to the CTS particles owing to their considerably larger sizes. However, empirical models for core-shell spheres and ellipsoids could be readily fit to the experimental data through the low and middle-q regime with a polydispersity term included, using calculated scattering length densities (SLDs) for the lipid and DNA components in X-rays and a fixed lipid bilayer depth of 54 Å. In the fitting, the resulting particle radii determined are largely consistent with the other measures reported herein (**Fig. 3J**).

As seen in **Fig. 3G**, both samples show overlapping but distinguishable peaks. For the CTS particles, these are the peaks at *q*=0.10 $Å^{-1}$ and 0.12 $Å^{-1}$, while for the standard particles these are the peaks at q=0.115 $Å^{-1}$ and 0.125 $Å^{-1}$. Using the relationship $d=2\pi/q$, where *d* is the distance between the repeat lipid-DNA structures, the peaks indicated organized structure at *d* = 59.8 Å and 52.3 Å respectively for the CTS particle and 54.6 Å and 52.3 Å for the standard particles respectively (**Table 1**). The pattern of the Braggs peak in this data provides direct information on the structural arrangement through the reciprocal spacings between peaks. Inverse hexagonal phases (hexosomes) have peaks spaced in the pattern of √1, √3, √4.. and so on, while bicontinuous particles (cubosomes) have different integral spacings [23, 24] (√1, √2, √3..). In the CTS data, the *q*=0.10 $Å^{-1}$ primary peak is readily assigned to a √1, √2, √3 spacing, indicative of cubosome phases (C), with corresponding peaks at *q*=0.15 $Å^{-1}$ and 0.18 $Å^{-1}$. The overlapping primary peak at *q*=0.12 $Å^{-1}$ is readily assigned to corresponding peaks spaced in the pattern of √1, √2, √3, at *q*=0.18 $Å^{-1}$ and 0.22 $Å^{-1}$. Several additional weak peak features could not be assigned. In addition to primary peaks, a broader and less well-defined shoulder in the profile at *q*=0.06-0.09 $Å^{-1}$ is observed which can be assigned to a higher order and more disordered phase. In contrast to the CTS structure, the standard LNP is better assigned with peak integrals consistent with an inverse hexagonal phase ($H_{||}$), with the *q*=0.115 $Å^{-1}$ peak readily assigned corresponding peaks at *q*=0.20 $Å^{-1}$ and 0.23 $Å^{-1}$. The overlapping peak at 0.125 $Å^{-1}$ could be assigned as an additional cubosome phase with corresponding peaks at *q*=0.18 $Å^{-1}$ and 0.22 $Å^{-1}$, and like with the CTS particle, a region of disorder between *q*=0.05-0.1 $Å^{-1}$ could also be assigned. These X-ray analyses indicate that the much larger CTS particles feature a cubosome/cubic structure very distinct from the canonical inverse hexagonal phases that define the smaller standard LNPs.

CTS LNPs enhance DNA transfection by orders of magnitude

Having confirmed the improved DNA loading characteristics and unique structural properties of CTS LNPs, we next demonstrated correlations between these structural features

and improved transfection, addressing the original goal of developing MSM and the CTS design. In RAW macrophages, we compared luciferase expression from plasmid DNA delivered via CTS LNPs vs standard DNA LNPs. CTS LNPs yield >10x higher expression than standard LNPs, and levels comparable to mRNA LNPs (**Fig 4A**). Comparing transfection efficiency, quantified as % of cells that are transfected by plasmid encoding GFP, CTS DNA LNPs outperform standard LNPs by three-fold (**Fig 4B**). In HeLa epithelial cells, CTS DNA LNPs yield ~150-fold higher luciferase expression than standard DNA LNPs (**Fig. 4D**), and double the transfection efficiency (**Fig. 4E**). Thus, compared to standard LNP formulations and single-step mixing, using MSM to create CTS LNPs improves protein expression from DNA cargo by 1-3 orders of magnitude.

In results presented up to this point in the manuscript, CTS LNPs are made using dilution cartridges with 3 channels in NanoAssemblr™ Ignite™ nanoparticle formulation systems. CTS LNPs can also be obtained by an in-house fabricated microfluidic device (**Fig 2B, Supplementary Fig 4, Supplementary Table 1**). We have screened a range of CTS LNP formulations varying the weight:weight ratio of shell lipids:pDNA, and have achieved results comparable to CTS LNPs prepared by NanoAssemblr in terms of size, PDI, DNA entrapment efficiency, and levels of luciferase expression. This shows that diverse microfluidic devices can generate CTS structures, but they all use MSM.

We had originally hypothesized that the CTS process would primarily work via benefits of compact DNA packaging, enhancing cytoplasmic trafficking and nuclear entry. However, another possibility is that CTS LNPs might affect LNPs' endosomal escape, which is typically the rate limiter for LNPs' transfection of mRNA [25]. To test this, we applied the same MSM CTS design for mRNA delivery and tested the protein expression level of CTS-mRNA LNPs in both RAW and HeLa cells, figuring out that the augmentation of expression of CTS-mRNA LNPs is 2-4 fold, compared to standard mRNA LNP (**Fig. 4C and 4F**). The enhanced mRNA expression indicates that CTS design alleviates the hurdles imposed by endo/lysosomes including inefficient endosomal escape. However, the expression improvement in the mRNA system is much less than the multiple orders of magnitude improvement for DNA. This could give real mechanistic insight: the bulk of CTS's benefits for DNA delivery is DNA-specific. This lowers the probability that CTS predominantly improves DNA transfection via effects on endosomal escape.

To quantify endosome escape events, we transfected HeLa cells with a galectin (Gal)-9-GFP plasmid and monitored LNP-mediated endosomal disruption (**Fig. 4G**). Galectins are primarily expressed in the cytosol and can be recruited to endosomes when membrane are damaged. Under baseline conditions, cells showed diffuse cytoplasmic Gal-9-GFP distribution [26]. Upon treatment with different LNP formulations, we observed distinct Gal-9-GFP puncta formation, indicating sites of endosomal membrane disruption (**Fig. 4H**). Quantification revealed that CTS LNPs induced higher Gal-9-GFP puncta formation than standard LNPs (**Fig. 4I**). However, this modest (though statistically significant) enhancement in endosomal escape cannot fully account for the 1-3 orders of magnitude improvement in transfection observed with CTS LNPs.

We next examined nuclear delivery kinetics using fluorescently labeled DNA. Live-cell imaging in HeLa cells revealed that CTS LNPs achieved nuclear accumulation rates comparable to Lipofectamine over a 60-minute period (**Fig. 4J**). Quantitative analysis showed nearly identical uptake profiles for both delivery systems (**Fig. 4K**), suggesting that while CTS LNPs match the nuclear delivery efficiency of this gold-standard transfection reagent, additional mechanisms beyond endosomal escape and nuclear entry must contribute to its superior transfection capabilities.

Co-loading CTS DNA LNPs with STING inhibitors further increases expression and enables in vivo expression peaks comparable to mRNA LNPs

Before moving CTS DNA LNPs *in vivo*, it was essential to address whether their DNA cargo activates intracellular DNA-sensors, especially cGAS-STING. Our previous work has shown that standard DNA LNPs strongly activate STING *in vivo*, leading to significant toxicity upon intravenous administration [4], and represses translation [27].

We had initially hypothesized that the CTS structure would provide enhanced protection of DNA through compaction in the core structure, shielding it from both cGAS-STING sensing and DNase degradation after endosomal escape (**Fig. 1A**). However, our findings indicate CTS LNPs' improved endosomal escape (**Fig 4G-I**) may actually increase cytosolic DNA accumulation over time, enhancing activation of DNA sensors like cGAS-STING. To test this, we incubated RAW macrophages with CTS DNA LNPs, standard DNA LNPs, or Lipofectamine with DNA and measured STING activation by immunostaining of phosphorylated STING [28]. We found that CTS LNPs indeed activated STING more strongly than standard LNPs, reaching levels comparable to Lipofectamine DNA delivery (**Fig. 5A-B**).

To mitigate STING activation, we loaded our CTS DNA LNPs with C-178, a small molecule STING inhibitor that covalently binds to Cys91, which is the same mechanism employed by mammal's endogenous STING inhibitors, nitrated lipids (**Fig. 5C**) [29]. C-178 was efficiently incorporated during CTS LNP synthesis, with a drug entrapment efficiency of 97.5% and drug-to-lipid molar ratio of 0.025. The loading of C-178 did not affect DNA entrapment efficiency. CTS LNPs loaded with C-178 effectively suppressed STING-mediated immune responses, as evidenced by complete elimination of IFN-β production in RAW macrophages (**Fig. 5D**). Importantly, C-178 co-loading enhanced transgene expression by approximately 4-fold in RAW macrophages and 20-fold in HeLa cells, compared to CTS LNP only (**Fig. 5E-F**).

Having solved the STING activation issue, we next evaluated STING-inhibiting C-178-loaded CTS DNA LNPs in challenging primary cell types. In mouse embryonic fibroblasts, C-178-loaded CTS DNA LNPs significantly outperformed Lipofectamine in transfection efficiency (**Fig. 5G-H**). Similarly, in primary cortical neurons, traditionally considered highly resistant to transfection, our formulation achieved superior gene delivery compared to Lipofectamine and preserved neuron morphology (**Fig. 5I-J**).

In vivo studies demonstrate that CTS DNA LNPs without C-178 enhance liver luciferase expression 5-fold over standard DNA LNPs (**Fig 5K-L**), but also induce significant toxicity leading to mortality (**Fig 5M**). Loading CTS LNPs with C-178 eliminates this toxicity while maintaining high transgene expression. A 5 ug dose of plasmid DNA in CTS DNA LNPs loaded with C-178 achieved orders of magnitude superior expression to a 25 ug dose in standard LNPs – despite the 5-fold reduction in dose. C-178-loaded CTS DNA LNPs produced peak expression levels approaching those of mRNA LNPs (**Fig 5N**), but with the crucial advantage of sustained expression (**Fig 5O**). The ability to achieve mRNA-like expression peaks with a reduced DNA dose, while maintaining long-term expression, makes CTS DNA LNPs very promising for treating chronic diseases.

DISCUSSION:

A long-standing goal in genetic medicine is to control gene expression in the diseases with the greatest burden on society: common chronic diseases. These diseases include the top causes of death like atherosclerosis, heart failure, and chronic obstructive pulmonary disease (COPD), as well as the top causes of illness and disability, such as Alzheimer's disease, chronic pain, and chronic kidney disease [30]. Unfortunately, genetic medicine tools have thus far been best suited to either rare monogenic diseases (AAV and CRISPR) or vaccines (mRNA LNPs). By contrast, DNA LNPs offer unique advantages that make them particularly well-suited for treating common chronic diseases: they can express or knockdown (by expressing short hairpin RNA [shRNA]) even large cargo genes because they impose no major cargo capacity constraint (unlike AAV's rigid capsid) [31]; maintain expression for ~6 months per dose (unlike the hours of expression with mRNA LNPs) [30]; achieve genetically-encoded cell-type specificity with

inclusion of large promoter regions (not possible with mRNA LNPs); avoid permanent integration or disruption of the genome (unlike AAV and CRISPR) [32]; minimize immunogenicity (unlike AAV) [32]; and leverage existing mRNA LNP targeting technologies. Thus, DNA LNPs can, with continued development, fill the greatest gap in genetic medicine, opening up therapy for dozens of common chronic diseases.

However, two major problems have historically limited DNA LNPs' clinical translation. First, DNA LNPs were noted for decades to be extremely toxic, which we solved in our recent work in which we co-loaded inhibitors of STING [4]. Second, standard DNA LNPs express proteins more poorly than mRNA LNPs and AAVs by orders of magnitude. In this study, we remedy this poor expression by the invention of multi-stage mixing (MSM) to create core-then-shell (CTS) DNA LNPs that express at 2-3 logs higher levels than standard DNA LNPs. With co-loading of the STING inhibitor C-178 into CTS DNA LNPs, we demonstrate improvements in transfection in multiple cell lines, multiple primary cell types considered to be “difficult-to-transfect”, and *in vivo* in mice. Thus, CTS DNA LNPs express genes at levels comparable to the gold-standard mRNA LNPs, but without mRNA’s limitations of a half-life of hours and lack of promoter regions.

Importantly, the CTS LNPs developed here represent a fundamentally different approach from traditional core-shell nanoparticles created through layer-by-layer (LbL) techniques. While LbL methods typically involve sequential deposition of oppositely charged materials onto a preformed core [33], our multi-stage mixing (MSM) approach employs a sophisticated microfluidic design that achieves two critical innovations simultaneously: (1) controlled compact packaging of DNA using precisely titrated DNA-condensing agents that facilitate nuclear entry; (2) rapid capture of thermodynamically metastable core matrices by lipid shells before aggregation can occur. The microfluidic architecture is crucial to this process. Traditional LbL requires multiple separation and purification steps between layer additions, which can lead to material loss and batch-to-batch variability [33]. In contrast, our MSM system achieves precise spatiotemporal control over the mixing process in a continuous flow format. The first mixing stage creates DNA-lipid complexes with moderate compacting - critically maintaining an N:P ratio below 2 to avoid over-condensation that would inhibit nuclear entry [12]. The second stage rapidly envelopes these nascent cores with a lipid shell before they can grow beyond the optimal size range. This process occurs in milliseconds, preventing the formation of large aggregates (>2000 nm) that typically plague attempts to create DNA-lipid cores through bulk mixing methods.

Our MSM approach offers distinct advantages over conventional core-shell particle synthesis through its precise control over the stoichiometry of the compact lipoplex DNA core, allowing optimization for nuclear transport. The system enables capture of metastable intermediates that would be impossible to achieve through equilibrium processes, while maintaining continuous flow production that enhances reproducibility and scalability. Compared to multi-step LbL processes, our method minimizes material loss and prevents aggregation through rapid shell formation.

While we have shown the CTS structure massively improves transfection, there is great need for future work deeply exploring the mechanisms of CTS’s improved efficacy. We were guided in our design of CTS by the hypothesis that compactifying DNA into a core would protect it from intracellular DNases, and enable it to pass more easily through the viscous cytosol and the narrow nuclear pore complex (**Fig. 1A**). However, proving whether or not these are indeed the mechanisms of CTS’s improved efficacy will require additional studies. Thus far, we have a few glimpses at the mechanisms. First, we found that it is essential to maintain DNA in the B-form, by optimizing the buffers in which DNA is formulated into LNPs and into which LNPs are dialyzed following synthesis. Second, we found that CTS improves mRNA LNPs’ transfection, but only by ~2-fold, which is much less than ~1,000-fold improvement by CTS for DNA LNP’s transfection. Third, we found that CTS improves endosomal escape (measured by Gal-9-GFP

puncta), but only by <2-fold. Fourth, we found that the time course of nuclear translocation of DNA is similar for CTS DNA LNPs and Lipofectamine. These four observations allow us to roughly estimate the relative contributions of different mechanisms to CTS's improved transfection: maintenance of the B-form plays a moderate role; improved endosomal escape plays a modest role (based on Gal-9 and mRNA expression data); and CTS allows rapid translocation to the nucleus.

While these tentative conclusions on mechanism are consistent with our initial hypothesis, we need more definitive mechanistic studies in the future. Such studies could include comparing CTS vs standard DNA LNPs in the following ways: measuring degradation of cargo-DNA after it enters the cell, including whether the DNA is partially damaged (nicked, linearized, or conformational changes); tracking the movement of cargo-DNA through the cytosol and nuclear pore complex, especially after plasma membrane permeabilization (to eliminate the effect on endosomal escape); and modifying CTS to produce larger or smaller cores, and compactify the DNA with different cations or other species, to probe structure-function relationships. Such mechanistic studies will not only elucidate key science in genetic medicine and material science, but also guide further practical engineering of MSM and CTS LNPs.

Indeed, MSM and CTS LNPs may open up a vast design space of materials for genetic medicine. Customized MSM designs may allow for multiple shell layers. Within just the CTS architecture, there is tremendous room for optimization, possibly allowing loading of chemical species that would normally partition out of LNPs. For example, we can change out the molecules used to condense the DNA and vary the microfluidic design to change the size and material properties of the LNPs. Finally, there is exciting work to be done to scale-up the manufacturing of MSM and CTS, which may be done with highly parallelized microfluidics [34, 35], or perhaps with macro-scale mixers like the confined impinging jet mixers used for the COVID vaccines [36].

With continued innovation of MSM and CTS LNPs, it is possible to foresee a time when DNA LNPs achieve their promise of safe, long-term control of expression of any protein. Such DNA LNPs would be able to treat a vast number of common chronic diseases. All of this can be made possible by applying novel materials engineering techniques like MSM to LNPs.

MATERIALS AND METHODS:

Material

SM-102 was purchased from Echelon Biosciences (Ontario, Canada). 18:0 PC (DSPC, 1,2-distearoyl-sn-glycero-3-phosphocholine), DMG-PEG 2000 (1,2-dimyristoyl-rac-glycero-3-methoxypolyethylene glycol-2000), 18:1 (Δ9-Cis) PE (DOPE), 18:1 TAP (DOTAP), 18:0 PE-DTPA and cholesterol were purchased from Avanti Polar Lipids (Alabaster, AL). RAW 264.7, HeLa cells, and mouse embryonic fibroblasts (MEFs) were purchased from American Type Culture Collection (Manassas, VA). Reporter lysis buffer and luciferin assay solution were purchased from Promega (Madison, WI). Plasmid DNA (pDNA) was purchased from Aldevron (<0.1 EU/µl endotoxin level). 5moU nucleoside-modified firefly luciferase mRNA was purchased from TriLink BioTechnologies. Indium-111 chloride (In-111) was purchased from BWXT Medical (Ottawa, Canada). Sodium iodine (I-125) was purchased from PerkinElmer (Waltham, MA). All other chemicals and reagents were purchased from Fisher Scientific (Hampton, NH), unless otherwise noted.

Animals

All animal studies were carried out in accordance with the Guide for Care and Use of Laboratory Animals under the protocol approved by the University of Pennsylvania Institutional Animal Care and Use Committee, and conformed to all relevant regulatory standards. Naive C57BL/6 mice (male, aged 6-8 weeks, 23-25g), naive BALB/c mice (female, aged 6-8 weeks,

23-25g) were procured from the Jackson Laboratory (Bar Harbor, ME). The animals were housed in a controlled environment maintained at temperatures between 22–26 °C, with a 12/12-hour light/dark cycle, and provided with access to food and water.

Cell culture

RAW264.7 mouse macrophages were cultured in Dulbecco's modified Eagle's medium (DMEM) with 10% heat-inactivated fetal bovine serum (FBS) and 1% penicillin/streptomycin (PS). HeLa cells were cultured in Eagle's Minimum Essential Medium (EMEM) supplemented with 10% FBS and 1% PS. Mouse embryonic fibroblasts (MEFs) were cultured in DMEM supplemented with 10% FBS, 2 mM L-GlutaMAX, 1X non-essential amino acids, 1 mM sodium pyruvate, 10 mM HEPES, 100 U/mL penicillin, 100 mg/mL streptomycin. All cells were incubated with 5% CO_2 at 37°C.

LNP Synthesis

LNPs were formulated using NanoAssemblr Ignite nanoparticle formulation systems (Precision Nanosystems, Vancouver, Canada), or using the microfluidics device designed in-house (**Fig. 2B**). The aqueous phase was made in different buffers including 50 mM citrate buffer (pH 4.0), Tris-acetate-EDTA (TAE), Tris-buffered saline (TBS), and HEPES with pDNA. For standard LNPs, an organic phase containing a mixture of lipids dissolved in ethanol at a designate molar ratio (**Fig. 1C**) was mixed with the aqueous phase containing DNA, at a flow rate ratio of 1:3 and at a total lipid to nucleic acid weight:weight ratio of 40:1. For CTS LNPs, channel 1 (core lipid phase) contains lipid mixture of DOPE and DOTAP; channel 2 (shell lipid phase) contains lipid mixture of ionizable lipid, DSPC, PEGylated lipid and cholesterol at a designated molar ratio (**Fig. 2A**); channel 3 (core aqueous phase) is pDNA in aqueous buffer. 3 channels were mixed at a flow rate ratio of 1:1:3. For drug-loaded CTS LNPs, STING inhibitor C-178 was added to channel 2.

LNPs were dialyzed against 1X PBS or 1X PBS containing $MgCl_2$ for 2 hours. Mg^{2+} concentration in the dialysis buffer corresponds to its concentration in the DNA-containing aqueous buffer, unless otherwise stated. After dialysis, LNPs were sterilized using a 0.22 µm filter, and stored at 4 °C for later use.

In-House Microfluidics Device Fabrication

A custom, dual-stage microfluidic mixer was fabricated in the Quattrone Nanofabrication Facility at the University of Pennsylvania. Design of the device was completed in AutoCAD (Autodesk, San Rafael, CA). Briefly, using a mask aligner, each layer of the multilayer architecture was photolithographically patterned onto a 100mm silicon wafer (ID 775; University Wafer, South Boston, MA) spray coated with S1805 photoresist (Dow, Midland, MI). After patterning and development, deep reactive ion etching (SPTS Rapier Si DRIE, Newport, UK) was performed. After the silicon was patterned and etched, the device was anodically bonded to a 100-mm Borofloat 33 glass wafer (ID 517; University Wafer) using an EVG 510 Wafer Bonding System (EVG Group, Oberosterreich, Austria).

Dual-valve pressure regulators (Alicat Scientific, Tucson, AZ) were used to pressurize 15mL vessels (Elveflow, Paris, France), with outputs mechanically coupled to the input ports of the microfluidic mixer. Separate inputs were provided for the ethanol and aqueous phase components, to allow for a two-step nanoprecipitation. The micromixer accommodated individual mixing of constituent components of the ethanol and aqueous phases to separately form the core and shell, which then combined and underwent further mixing. Pressures were chosen to allow the total flow rate through each input to combine to a total flow rate of 1.2mL/min. CTS LNP samples were collected directly into a dialysis cassette (Thermo Fisher, Waltham, MA), and dialyzed against 1X PBS containing 4 mM $MgCl_2$ for 2 hours.

LNP Characterization

Hydrodynamic nanoparticle size, polydispersity index (PDI), and bulk zeta potential of LNPs were measured by dynamic light scattering using Zetasizer Pro ZS (Malvern Panalytical, Westborough, MA). Distribution of zeta potential of individual LNP was measured by ZetaView instrument by Particle Metrix (Inning am Ammersee, Germany).

Encapsulation efficiency and concentration of pDNA or mRNA were measured using a Quant-iT-PicoGreen, or Ribogreen, respectively. 50 µL of TE buffer and 50 µL of 2% Triton X-100 (in TE buffer) were added in duplicates to a black bottom 96-well plate. LNP formulations were diluted in the TE buffer, and 50 µL of each formulation was added to the TE buffer and 2% Triton X-100. After 10 minutes of incubation time, RiboGreen or PicoGreen reagent was diluted 1:100 or 1:200, respectively, in the TE buffer and added to each well. Picogreen fluorescence was measured at excitation of 480 nm and emission at 520 nm, and RiboGreen signal was measure using an excitation 485 nm of and emission of 528 nm by a plate reader (Spectramax M2; Molecular Devices, San Jose, CA).

Drug encapsulation was measured by high-performance liquid chromatography, and drug entrapment efficiency was calculated as weight of loaded drug in LNPs over weight of total drug added into LNP formulation.

Cryo Electron Microscopy

To prepare samples for cryo-EM imaging, lacey carbon–coated 300 mesh copper grids (Electron Microscopy Sciences) were glow discharged at 15 mA for 30 s with the PELCO easiGLOW glow discharge system (Ted Pella). Then, 8 µL of sample was applied to the grids. The grids were blotted with filter paper and plunge frozen in liquid ethane using Vitrobot Mark IV, under 4 °C and 100% humidity. The grids were kept in liquid nitrogen until imaging. Cryo-EM images were collected with Titan Krios Cryo-TEM (ThermoFisher).

Circular Dichroism Spectroscopy

All CD experiments were carried out using Jasco 1500 CD spectrometer. The following parameters were used: range 200-320 nm, data pitch = 1 nm, CD scale = 200 mdeg/0.1 dOD, FL scale = 200 mdeg/0.1 dOD, Digital Integration Time = 1 sec, bandwidth = 1 nm. pDNA were measured at the concentration of 30 µg / mL. Buffer solutions alone were used as blanks to establish baselines for correction. Normalized raw CD data were used for plotting and analysis.

Differential Scanning Calorimetry

Samples of LNPs were prepared for calorimetry measurements at particle concentrations of 3-5e11 nanoparticles per mL in PBS. PBS was used as a reference solution for all differential scanning calorimetry measurements. Reference PBS was drawn from the same aliquot used to dilute nanoparticle samples. Lipid nanoparticle suspensions and reference solutions were heated from 4°C to 130°C at a target rate of 1°C per minute in a TA Instruments Nano DSC operating in scanning mode. Background measurements of reference PBS vs. reference PBS were obtained to confirm stability of the measurements and reference vs. reference thermograms were subtracted from all LNPs vs. PBS reference thermograms. Sigmoidal fits were applied to baselines of background-corrected thermograms in TA Instruments NanoAnalyze software. After baseline subtraction, thermogram data were normalized to instantaneous scan rate and molar concentration of nanoparticles as measured by nanoparticle tracking analysis. The resultant molar heat capacity thermograms were integrated to yield enthalpy data or normalized to temperature then integrated to yield entropy data. Enthalpy, entropy, and Gibbs energy of any phase transitions were extracted from this data.

Small Angle X-ray Scattering

Dynamic Light Scattering. A Nanobrook Omni particle sizer (Brookhaven Instruments Corporation, Holtsville, NY, USA) was used to record data at 25°C in polystyrene 1-cm cells using a standard diode laser at 640 nm, with scattering recorded at an angle of 90°. Three scans were recorded for each sample and hydrodynamic radii (R_h) were calculated using the BIC Particle Solutions software v3.6.0.7122.

SEC-MALS. 100 µL of DNA LNP at a particle concentration of ~10^{11} particles were injected and eluted isocratically at 0.2 ml/min from a 7.8 mm TSKgel G6000PWxl-CP sizing column equilibrated in 1X PBS at room temperature. Absolute molar mass of the DNA LNPS was determined in-line using multi-angle light scattering. Light scattering from the column eluent was recorded at 18 different angles using a DAWN-HELEOSII MALS detector (Wyatt Technology Corp.) operating at 658 nm. Eluent concentration using a mass averaged dn/dc value of 0.16 cm3/g was determined using an in-line Optilab T-rEX Interferometric Refractometer (Wyatt Technology Corp.). The weight-averaged molar masses of species within defined chromatographic peaks were calculated using the ASTRA software version 8.2.2 (Wyatt Technology Corp.), by construction of Debye plots (KC/Rθ versus. $\sin^2[\theta/2]$) at one second data intervals. The weight-averaged molar mass was then calculated at each point of the chromatographic trace from the Debye plot intercept and an overall average molar mass was calculated by weighted averaging across the peak. Normalization coefficients for diode counting efficiency were obtained using a BSA standard.

SEC-SAXS. *Synchrotron Size-Exclusion Chromatography in line with Small Angle X-ray Scattering*. Size-exclusion chromatography (SEC)-SAXS data were collected at beamline 16-ID (LiX) of the National Synchrotron Light Source II (Upton, NY) [37]. Data were collected at a wavelength of 1.0 Å in a three-camera configuration, yielded accessible scattering angle where $0.006 < q < 3.0$ Å^{-1}, where q is the momentum transfer, defined as $q = 4\pi \sin(\theta)/\lambda$, where λ is the X-ray wavelength and 2θ is the scattering angle; data to $q<0.5$ Å^{-1} were used in subsequent analyses. 100 µL of DNA LNP at a particle concentration of ~10^{11} particles were injected and eluted isocratically at 0.2 ml/min from a 7.8 mm TSKgel G6000PWxl-CP sizing column equilibrated in 1X PBS (Invitrogen), at room temperature. Eluent from the column flowed into a 1 mm capillary for subsequent X-ray exposures at 1-s intervals. Plots of intensity from the forward scatter closely correlated to in-line UV and refractive index (RI) measurements.

SAXS Analysis. SEC-SAXS data sets were analyzed in the program RAW [38]. Buffer subtracted profiles were analyzed by singular value decomposition (SVD) and the ranges of overlapping peak data determined using evolving factor analysis (EFA) as implemented in REGALS [39]. The determined peak windows were used to identify the basis vectors for each component and the corresponding SAXS profiles were calculated. When manually fitting the pair distribution function P(r) using the program DIFT[40], the maximum diameter of the particle (D_{max}) was incrementally adjusted to optimize χ^2 figures, to minimize the discrepancy between the fit and the experimental data to a $q_{max} \leq 8/R_g$, and to optimize the visual qualities of the distribution profile.

Deconvolution of the primary Braggs peaks in SAXS were performed using multiple Lorentz with the built-in functions implemented in OriginPro 2024b (Northampton, MA, USA), as previously described [24]:

$$y = y_0 + (2*area/\pi)*(width/(4*(x - x_c)2 + width^2))$$

where y_0 is an offset and was set to the X-ray baseline. x_c is a center of function and corresponds to the center of the SAXS peak. In the fitting, the peak position was fixed and the area and width of the peaks were not restrained. Peaks were assigned to inverse hexagonal ($H_{||}$) or lamellar (L_α) phases based on peaks corresponding to the first order Bragg peak and corresponding peaks at integral increments [23].

SASView (www.sasview.org) was used to fit experimental data to empirical models for core-shell sphere and ellipsoid models. In this fitting, scattering length densities (SLDs) were fixed to calculated values and the shell diameter to that of a lipid bilayer (54 Å). The SLDs for

the component parts of the DNA LNP formulations used in this fitting were calculated using MULCh [41].

DENSS [42] was used to calculate the *ab initio* electron density map directly from the DIFT output. Twenty reconstructions of electron density were performed in the slow mode with default parameters and subsequently averaged and refined. Reconstructions were visualized using PyMOL 2.5.2 Molecular Graphics System (Schrodinger, LLC, New Your, NY, USA) with five contour levels of density rendered with these respective colors: 15σ (red), 10σ (green), 5σ (cyan), 2.5σ (blue), and -0.7σ (blue). The sigma (σ) level denotes the standard deviation above the average electron density value of the generated model.

In vitro LNP transfection

HeLa cells and RAW 264.7 macrophages were seeded in 96-well plates and incubated overnight (seeding density of $5x10^3$ and $5x10^4$ cells/well, respectively), and treated with 200 ng/mL or 500 ng/mL of luciferase-pDNA LNP, respectively. Following 24 hour LNP treatment, 10% cell counting kit-8 (CCK-8, Enzo Life Sciences) reagent in complete medium was added to cells for 30 minutes incubation and run a colorimetric assay to measure cell viability, according to manufacturer's protocol. To test the transfection efficiency of luciferase-pDNA LNP, cells were lysed by cell culture lysis reagent and cell lysates were tested using luminometer upon adding luciferase assay substrate.

MEFs were seeded in ibidi μ-slide 8 well glass bottom chamber (Fitchburg, WI) at the density of $2x10^4$ cells/well. 200 ng/mL of eGFP pDNA LNP or Lipofectamine were added in complete medium and incubated for 24 hours. eGFP-positive cells were imaged using Leica Stellaris 5 confocal microscopy (Leica Microsystems).

For the primary neuronal culture, E16-E18 embryos were collected for neuronal culture. Single cells were obtained and seede in 8 well glass bottom chamber at $6x10^4$ cells/well. Neurobasal Plus medium (Gibco, #A3582901) with B27 supplement (Gibco, #A3582801), 1 x GlutaMax and 1% P/S was used for neuronal maintenance. Replace half of the medium every 3 days. On day 3, 5 uM AraC was used for inhibiting proliferating cells. At day 11, neurons were treated with 200ng/mL of eGFP pDNA LNP or Lipofectamine, and were imaged 24 hours later.

Cytokine measurements were carried out on cell culture medium from RAW macrophages after 4-hour treatment, with IFN-β ELISA kit (Abcam), according to the manufacturer's instructions.

Radiolabeling Biodistribution

For biodistribution studies, LNPs or fibrinogen were traced with In-111 or I-125, respectively. LNPs were formulated as described above with 0.1 mol% of 18:0 PE-DTPA using metal-free buffers. Trace metals were removed from the buffers using a Chelex 100 resin, per manufacturer's instruction. In-111 was mixed with LNPs at a specific activity of 1 μCi of In-111 per 1 μmol of lipid. The mixture was incubated at room temperature for 30 minutes. Fibrinogen was radiolabeled with I-125 using the Iodogen method. Glass tubes coated with 100μg of Iodogen reagent were incubated with fibrinogen (2 mg/mL) and I-125 (115 μCi per μg protein) for 5 minutes on ice. Unincorporated In-111 or I-125 was removed with a Zeba 7kDa desalting spin column (ThermoFisher Scientific). Thin layer chromatography was used to confirm radiolabeling efficiency. All materials were confirmed to have >90% radiochemical purity prior to use.

To trace distribution, fibrinogen was injected 2 minutes prior to LNP intravenous injection. 30 minutes later, blood and organs were harvested, and the radioactivity was quantified with a gamma counter (Wizard2, PerkinElmer). The gamma data and organ weights were used to calculate the tissue biodistribution injected dose per gram.

DNA uptake and nuclei colocalization

DNA was labeled with SYBR Green by mixing SYBR Green I Nucleic Acid Gel Stain (Invitrogen, Waltham) at 2000X with 1 mg/mL pDNA at room temperature for 30 minutes. Free dye was removed by Zeba desalting spin column. DNA concentration and fluorescent intensity was confirmed by NanoDrop Microvolume Spectrophotometers (Thermo Scientific). SYBR Green labeled pDNAs were then used to either mix with Lipofectamine 2000 to form lipoplexes or to make pDNA LNPs following previously mentioned LNP synthesis procedure.

HeLa cells were seeded in ibidi µ-slide 8 well glass bottom chamber at a density of $2x10^4$ cells/well and grew overnight. Hoechst 33258 (Cayman Chemical) was added 10 minutes prior to LNP treatment. Cells were treated with 2000 ng/mL of SYBR Green-labeled pDNA LNPs or pDNA-Lipofectamine 2000 in OPTI-MEM medium. Time-lapse imaging was acquired under 5% CO_2 at 37°C to trace DNA uptake and nuclei transport. For colocalization analysis, Fiji ImageJ software is used to perform nuclei mask and raw integrated density of SYBR green signal within the nuclei mask were measured and calculated.

Nanoparticle Tracking Analysis

mRNA and plasmid DNA was labeled using Label IT® Nucleic Acid Labeling Kit (MoBiTec GmbH, Goettingen, Germany) according to the manufacturer's protocol. Briefly, nucleic acid was mixed with *Label* IT® Reagent at the (w:v) ratio of 5:2, and reacted at 37 °C for 1 hour. Unreacted dye of DNA was purified using G50 Microspin Purification Columns. The labeled mRNA was purified by ethanol precipitation. The final concentration was determined using a NanoDrop Spectrophotometer.

Cy5 labeled mRNA and Cy3 labeled DNA were used to form LNPs to analyze nucleic acid payload in individual nanoparticles. Briefly, LNPs were diluted with deionized water and analyzed using nanoparticle tracking analysis through a Nanosight NS300 (Malvern Panalytical, Westborough, MA). Light scattering mode was used to determine total LNP concentration. Fluorescent mode was used to determine fluorescent nucleic acid loaded LNP concentration. The size of free fluorescent nucleic acid is below the instrument measurement limit, thus was not reported. Percentage of LNP loaded with nucleic acid was calculated as concentration of fluorescent LNP over that of total LNP.

Quantitative endosomal escape assessments by galectin-9 reporter cell

HeLa cells expressing mCherry-coupled galectin-9 (mCherry-GAL9) were obtained by transfection using plasmids encoding mCherry-galectin 9 (Addgene, Watertown, MA). The galectin-9 reporter HeLa cells were then cultured in ibidi µ-slide 8 well glass bottom chamber at a density of $2x10^4$ cells/well and grew overnight. Cells were dosed with 400 ng/mL of pDNA LNPs for 24 hours. After fixation with 4% paraformaldehyde (PFA), cells were stained with DAPI and imaged using confocal microscopy. Within individual cell regions of interest, galectin-9 puncta was analyzed via measuring the integrated density of mCherry signals using Fiji ImageJ software.

p-STING imaging and quantification

Raw macrophages were seeded in ibidi µ-slide 8 well glass bottom chamber at a density of $2x10^5$ cells/well and grew overnight. 1000 ng/mL of pDNA LNPs were used to treat cells for 4 hours. After treatment, cells were washed with PBS for three times and fixed with 4% paraformaldehyde. For phosphorylated STING staining, cells were permeabilized in 0.1% Triton for 10 minutes, and stained with primary antibody (Phospho-STING (Ser366), 1:200) in blocking buffer containing 10% bovine serum albumin at 4 °C overnight, followed by a secondary antibody (Alexa Fluor 594-conjugated goat-anti rabbit antibody, 1:500) at room temperature for 2 hours. Cell nuclei were labeled using DAPI. Images were acquired by confocal microscopy and mean fluorescent intensity of individual cells were measured by Fiji ImageJ software.

In Vivo Imaging System

LNPs were injected intravenously into the BALB/c mice. One dose of 10mg/kg baricitinib was injected intravenously 5 minutes prior to injection of C-178 loaded CTS DNA LNP. At the time of imaging, mice were intraperitoneally injected with 100 uL of 30 mg/mL D-luciferin sodium salt under 3% isoflurane-induced anesthesia, then placed in an IVIS Spectrum machine (PerkinElmer) belly up and imaged for whole body chemiluminescence every 0.2 minutes with automatically determined exposure time for 10-12 images, until the signal reached the peak intensity.

Statistics

All results are expressed as mean ± SEM unless specified otherwise. Statistical analyses were performed using GraphPad Prism 8 (GraphPad Software) * denotes $p<0.05$, ** denotes $p<0.01$, *** denotes $p<0.001$, **** denotes $p<0.0001$.

Acknowledgements

Research reported in this publication was supported by the Institute for RNA Innovation of the Perelman School of Medicine at the University of Pennsylvania (to J.N.), the PhRMA Foundation Postdoctoral Fellowship in Drug Delivery 2023 PFDL 1008128 (to Z.W), Grant R01-HL-157189 (to V.R.M), Grants R01-HL-153510, R01-HL160694, R01-HL164594 (to J.S.B).

K.G. acknowledges support from the Johnson Research Foundation and NIH Shared Instrumentation Grant S10-OD018483. The SV-AUC and light scattering experiments were performed at the Johnson Foundation Biophysical and Structural Biology Core Facility (University of Pennsylvania, Philadelphia PA). The SEC-SAXS data were obtained at 16-ID (LIX) at the National Synchrotron Light Source II, a U.S. Department of Energy (DOE) Office of Science User Facility operated for the DOE Office of Science by Brookhaven National Laboratory under Contract No. DE-SC0012704. This work benefited from the use of the SasView application, originally developed under NSF award DMR-0520547. SasView also contains code developed with funding from the European Union's Horizon 2020 research and innovation programme under the SINE2020 project, grant agreement No 654000.

We thank Electron Microscopy Resource Lab (RRID:SCR_022375) for their help with cryo-EM imaging, and Extracellular Vesicle Core for ZetaView analysis.

Table 1. Table of Parameters Determined by SEC-SAXS Analysis

Sample	Lorentz Fitting[A] | Peak 1					Lorentz Fitting[A] | Peak 2					IFT[B]	
	q (Å^{-1}) Peak 1	I_p (cm^{-1})	d (Å)	Area	FWHM	q (Å^{-1}) Peak 1	I_p (cm^{-1})	d (Å)	Area	FWHM	R_g (Å)	D_{max} (Å)
CTS	0.100	0.10	62.8	0.002	0.021	0.125	0.09	50.2	0.002	0.002	*n.d.*	*n.d.*
Std	0.115	0.13	54.6	0.004	0.021	0.127	0.11	49.4	0.002	0.012	156	419

n.d. - not determined

[A]Multiple Lorentz fitting was performed on profiles derived with characteristic first-order Braggs peak within q~0.05-0.25 Å^{-1}, using the program Origin.

[B]Inverse Fourier Transform (IFT) analyses were performed using DIFT[40] in conditions where $q_{min} * D_{max} \leq \pi$. In all experiments, q_{min} = 0.006 Å^{-1}.

Figure 1: Improving transfection by optimizing the buffer used during LNP synthesis to ensure DNA stability. A) DNA LNPs have 5 major hurdles to high protein expression: DNA structural perturbations during the LNP synthesis (#1); Upon cell uptake and endosomal escape, the DNA can be recognized by intracellular DNA sensors such as cGAS-STING (#2) and cleaved by DNases (#3); Finally, the DNA must travel through the cytosol (#4) and cross into the nucleus to engage in transcription (#5). The current study aims to employ structural modifications of DNA LNPs to overcome these hurdles. **B) Circular Dichroism (CD) Spectroscopy.** Testing how the buffer used during DNA LNP synthesis can change the fraction of DNA in the B-form. DNA was dissolved in either the most common buffer for mRNA LNP synthesis, citrate (pH 4), or TBS buffers (pH 6) with 4mM Mg^{2+}, then subjected to CD spectroscopy. The ellipticity signal at 245nm and 275 nm correlates with B-form DNA, and highest for the TBS buffers containing Mg^{2+}, and lowest for citrate. **C) Schematic illustration of making standard LNP**: LNP is formed by mixing of lipid mixture and DNA plasmid in aqueous buffer, followed by dialysis in PBS or PBS containing Mg^{2+} in correspondence to Mg^{2+} concentration in the aqueous buffer, unless otherwise noted. **D) Representative Cryo-EM** of DNA LNPs in citrate or optimized TBS buffers. Scale bar denotes 25 nm. **E, F) Effect of Mg^{2+} in LNP formulation on cell transfection.** A macrophage-like cell line (RAW 264.7) was transfected with DNA LNPs encoding luciferase, synthesized and dialyzed with the listed buffers. By far the highest expression was seen with TAE buffer containing Mg^{2+} and dialyzed against Mg^{2+} containing PBS. **G, H, I) Effect of pH and buffer in LNP formulation on macrophage transfection.** Comparing DNA expression in macrophages using 4 buffering molecules at pH 5 (G) and pH 6 (H) and with added Mg^{2+} (I), showing TBS with Mg^{2+} at pH 6 is the optimal buffer. **J, K, L) Effect of pH and buffer in LNP formulation on epithelial cell transfection.** Using an epithelial cell line (HeLa) produces the same general trends as seen in macrophages, with the exception that in the presence of Mg^{2+}, TAE outperforms TBS.

Figure 2: Multi-stage mixing (MSM) to produce core-then-shell (CTS) improves the encapsulation of nucleic acids. A) Schematic illustration of making CTS LNP. Instead of the standard single mixing stage LNPs have used for decades, CTS LNPs are made via multi-stage mixing. First, in the Core Stage, the DNA (aqueous buffer) is mixed via a microfluidic with an organic solvent containing a cationic lipid and helper lipid. This condenses the DNA into a "core." Immediately upon core formation, the cores are mixed with standard LNP lipids in the organic phase, to form the "shell". **B) Schematic illustration of in-house made microfluidic chip. C) Dynamic Light Scattering (DLS).** CTS LNPs are larger than standard (Std) LNPs, but have a lower polydispersity index (PDI). **D) ζ-Potential Analysis using ZetaSizer.** CTS LNPs are closer to neutral, measuring the bulk nanoparticle population. **E) DNA entrapment efficiency:** CTS LNP and standard LNP have similar DNA entrapment efficiency around 90%. **F, G, H) DNA cargo payload distribution in LNPs.** To evaluate the distribution of DNA within a population of LNPs, we used Nanoparticle Tracking Analysis (NTA) to trace particles using light scattering (right panels) and simultaneously measure DNA loading into each particle via fluorescently labeled DNA (left panels). In G & H, we plot the distribution of nanoparticle sizes, as measured by light scattering (solid lines) or DNA fluorescence (dashed). G shows that in standard LNPs, a low fraction of particles contain detectable DNA, while H shows that for CTS LNPs a very high fraction of nanoparticles contain DNA. **I) quantification of F-G**, showing that in standard LNPs, only ~50% of LNPs have detectable DNA, while 83% of CTS LNPs have detectable DNA. **J, K, L) RNA cargo payload distribution in LNPs.** NTA evaluation of mRNA payload in standard LNP vs CTS LNP shows similar trend as in DNA LNP. **M) Quantification of K-L**, showing that in standard LNPs, only 5% of LNPs have detectable RNA, while 98% of CTS LNPs have detectable RNA.

Figure 3: Multi-stage mixing dramatically changes the internal structure of DNA-LNPs, producing a distinct core vs shell. A) Representative Cryo-EM of core-then-shell (CTS) vs standard LNPs shows that CTS-LNPs created using multi-stage mixing (MSM) display distinct core and shell phases. The white bar shown denotes a length of 25 nm. **B) ζ-Potential Analysis.** We compared the ζ-potentials of two LNP formulations: the CTS lipid formulation (containing <2% DOTAP), made either with MSM or single-stage (traditional) mixing. Single-stage mixing (green) produces two very separate populations with very low magnitude potentials, one positive and one negative; by contrast, MSM (blue) produces CTS LNPs with a single broad distribution of potentials between 0 mV and -50 mV, like seen with the standard LNP formulation (no DOTAP, black). This demonstrates that MSM is critical to creating CTS LNPs. **C) Differential Scanning Calorimetry (DSC).** The molar heat capacity of CTS and standard LNP particles were determined. Standard LNPs (black line) display a broad profile and short peak, consistent with modestly stable population. In contrast, CTS-LNPs (blue line) shows two sharp peaks with a larger magnitude, consistent with a more uniform and well-ordered population of higher stability. **D) Dynamic Light Scattering (DLS).** Particle size distributions, normalized for intensity, as determined by DLS are shown as lognormal distributions, with CTS shown in blue and standard LNPs shown in black. CTS particles had a determined hydrodynamic radius (R_h) of 151 Å ± 2.3 (polydispersity index (PDI) = 0.14) compared to 80.2 Å ± 2.5 (PDI = 0.28) for the standard formulation. **E) Radius of Gyration Analysis (R_g) using Size-exclusion Chromatography In-line with Multiangle Light Scattering (SEC-MALS).** Shown is a double-y plot, where the left axis provides the normalized refractive index for eluant as a function of retention time for CTS particles (blue line), while the right axis provides on a log-scale the radius of gyration (R_g, in nm) of the CTS particles as determined using 18-angle light scattering (blue circles). Across the peak region analyzed, a R_g of 39.5 nm ± 5.5% was determined. A similar analysis could not be performed for standard LNP particles, as the particles were well below the size threshold needed for reliable determination of R_g. **F) Mass profiles using SEC-MALS.** Shown is a double-y plot, where the left axis provides the normalized refractive index for eluant as a function of retention time for standard (black line) and CTS particles (blue line), while the right axis provides on a log-scale the determined molar mass. Across the peak regions analyzed, a M_w of 23.7 MDa ± 2.1% was determined for CTS particles and 5.4 MDa ± 3.1% for the standard LNP particles. **G) Synchrotron Size-Exclusion Chromatography in-line with Small-Angle X-ray Scattering (SEC-SAXS).** Log-linear plots of SAXS data from standard LNPs (black line) and CTS particles (blue line), showing the decay of scattering intensity as a function of the scattering vector q (where $q=4\pi\sin\theta/\lambda$). Characteristic first-order Braggs peak features are observed between q=0.1-0.2 $Å^{-1}$. See Supplemental Figure 1 for additional information. **H) Multiple Lorentz Function analysis of Braggs peaks from SAXS of CTS Particles**. Shown as blue line are the SAXS data in a linear-linear plot, as a blue line. Multiple Lorentz fits were applied to deconvolute the data and are shown as dotted lines. The assignment of the cubosome phase peaks with the spacing of d=62.8 Å and corresponding peaks at integral values of $q^*\sqrt{2}$ and $q^*\sqrt{3}$. The overlapping peak at q=0.125 $Å^{-1}$ (d=50.2 Å) could additionally be assigned to corresponding integral peaks integral values of $q^*\sqrt{2}$ and $q^*\sqrt{3}$. **I) Multiple Lorentz Function analysis of Braggs peaks from SAXS of standard LNP Particles**. Shown as black line are the SAXS data in a linear-linear plot. Multiple Lorentzian models were applied to deconvolute the data and are shown as dotted lines. The assignment of the $H_{||}$ phase peaks with the spacing of d=54.6 Å and corresponding peaks at integral values of $q^*\sqrt{3}$ and $q^*\sqrt{4}$. The overlapping peak at q=0.127 $Å^{-1}$ (d=49.5 Å) could be related to a corresponding integral peaks $q^*\sqrt{2}$, suggesting an additional cubosome phase. **J) SASVIEW Analysis**. Fitting of I vs q data shows core-shell sphere (light grey line) and core-shell ellipsoid model (dark grey lines) fits with polydispersity term. Residuals of the fits are shown in the lower panel. In this fitting, scattering length densities (SLDs) were fixed to calculated values and the shell diameter to that of a lipid bilayer (54 Å). The SLDs for the component parts of the DNA

LNP formulations used in this fitting were calculated using MULCh. In the core-shell sphere model, a core radius of 101.8 Å ± 42.1 was determined (χ^2=2.7). In the core-shell ellispsoidal model fit, an equatorial core radius of 86.5 Å ± 86.9 and a long axis radius of 136.7 Å ± 332.5 was determined (χ^2=2.4) .

Figure 4: Core-then-shell LNPs enhance transfection by orders of magnitude via improving endosomal escape and rapidly localizing DNA to the nucleus. A-F) *In vitro* transfection with the listed LNPs in RAW macrophages (A, B, C) and HeLa epithelial cells (D, E, F) shows that comparing with lipofectamine, a gold standard benchmark for *in vitro* transfection. CTS DNA LNPs express 10-fold higher than standard DNA LNPs in RAW macrophages and 100-fold higher in HeLa cells, and equivalent to mRNA-LNPs. In addition, CTS LNP has significant transfection efficiency than Std LNP. Not only for DNA, CTS mRNA LNPs also enhance mRNA expression, compared to standard mRNA-LNPs. **G) Endosome escape events.** To measure endosomal escape events, HeLa cells were transfected with plasmids containing GFP-labeled galectin-9, which forms puncta around endosomes that have opened. **H) Representative image of Gal-9 reporter cells after LNP or lipofectamine treatment. I) Quantification of Gal-9 puncta.** The Gal-9-GFP puncta per cell were higher in CTS LNP compared to standard LNPs, and reached a similar level to the gold-standard Lipofectamine. **J) Representative image of time lapse of DNA uptake in HeLa cells. K) Quantification of DNA uptake.** To measure DNA uptake and import into the nucleus, DNA was fluorescently labeled with SYBR-Green, loaded into CTS-LNPs, and given to HeLa cells. The uptake into the nucleus via CTS LNPs is on a very similar time course to that of Lipofectamine. Scale bar denotes 50 µm.

Figure 5: Co-loading a STING-inhibitor into core-then-shell (CTS) DNA LNPs enables high-level, long-term expression of DNA LNPs in primary cells in culture and *in vivo*. A) Representative image of phosphate-STING (p-STING) signal in RAW macrophages after LNP or lipofectamine treatment**.** The cGAS-STING pathway detects cytosolic DNA and thereafter activates pathways involved in inflammation and repression of protein translation. To measure STING activity, we stained RAW macrophages with phospho-STING antibody. **B) Quantification of p-STING.** We found that CTS LNPs activate STING much more than standard LNPs, and to the same extent as Lipofectamine. **C) Schematic illustration of cGAS-STING activation pathway and C-178 function in inhibition of STING.** STING induces expression of IFN-β, which activates inflammation and represses translation. C-178 is a small molecule analog of the endogenous negative feedback on STING. **D) IFN- β level.** CTS DNA LNPs massively increase expression of IFN-β by RAW macrophages, but this is completely inhibited by co-loading C-178 into the CTS LNPs. **E, F) *In vitro* transfection of CTS LNP co-loading with C-178.** In both RAW macrophages and HeLa epithelial cells, C-178 co-loading improves protein expression. **G, H, I, J) Primary cell transfection by CTS LNPs.** Lipofectamine is the gold standard for *in vitro* transfection, but is inefficient with most primary cells. Here we measured expression, via GFP plasmids, in mouse embryonic fibroblasts (G, H), and mouse primary cortical neurons (I, J). In both cases, CTS LNPs co-loaded with C-178 had markedly higher transfection efficiency than Lipofectamine, and preserved neuron morphology. **K) Representative images from In Vivo Imaging System (IVIS).** Standard and CTS LNPs, without any STING inhibitor (e.g., C-178), were IV-injected into mice and luciferase expression was measured via IVIS at 24 hours. **L) IVIS image quantification.** CTS showed expression markedly above standard LNPs, but the CTS LNPs' expression was likely inhibited by STING expression. **M) Animal survival.** CTS LNPs without STING inhibition had 100% mortality within 3 days, but CTS LNPs co-loaded with C-178 had 0% mortality. **N) Day 1 IVIS image quantification.** After IV injection, standard DNA LNPs drive expression that is several orders of magnitude lower than mRNA LNPs, though we recently showed that these DNA LNPs

drive expression for more than 3 months, while LNP-delivered mRNA decays in days. However, CTS DNA LNPs with co-loaded C-178 show peak expression levels orders of magnitude higher than standard-DNA-LNPs, with the dose 5 times lower than standard-DNA-LNPs, and comparable to mRNA LNPs' peak. **O) Longitudinal quantification of DNA expression *in vivo.*** Scale bar denotes 50 µm.

REFERENCE:

1. Tenchov, R., et al., *Lipid Nanoparticles horizontal line From Liposomes to mRNA Vaccine Delivery, a Landscape of Research Diversity and Advancement.* ACS Nano, 2021. **15**(11): p. 16982-17015.
2. Pardi, N., et al., *Expression kinetics of nucleoside-modified mRNA delivered in lipid nanoparticles to mice by various routes.* J Control Release, 2015. **217**: p. 345-51.
3. Veiga, N., et al., *Cell specific delivery of modified mRNA expressing therapeutic proteins to leukocytes.* Nat Commun, 2018. **9**(1): p. 4493.
4. Patel, M.N., et al., *Enabling non-viral DNA delivery using lipid nanoparticles co-loaded with endogenous anti-inflammatory lipids.* bioRxiv, 2024.
5. Chaudhary, N., D. Weissman, and K.A. Whitehead, *Author Correction: mRNA vaccines for infectious diseases: principles, delivery and clinical translation.* Nat Rev Drug Discov, 2021. **20**(11): p. 880.
6. Dinis, T.B.V., F. Sousa, and M.G. Freire, *Insights on the DNA Stability in Aqueous Solutions of Ionic Liquids.* Front Bioeng Biotechnol, 2020. **8**: p. 547857.
7. Yu, L. and P. Liu, *Cytosolic DNA sensing by cGAS: regulation, function, and human diseases.* Signal Transduct Target Ther, 2021. **6**(1): p. 170.
8. Bai, H., et al., *Cytoplasmic transport and nuclear import of plasmid DNA.* Biosci Rep, 2017. **37**(6).
9. Wente, S.R. and M.P. Rout, *The nuclear pore complex and nuclear transport.* Cold Spring Harb Perspect Biol, 2010. **2**(10): p. a000562.
10. Corsi, J., et al., *DNA lipoplexes: formation of the inverse hexagonal phase observed by coarse-grained molecular dynamics simulation.* Langmuir, 2010. **26**(14): p. 12119-25.
11. Zheng, L., et al., *Lipid nanoparticle topology regulates endosomal escape and delivery of RNA to the cytoplasm.* Proc Natl Acad Sci U S A, 2023. **120**(27): p. e2301067120.
12. Akita, H., et al., *Effect of the Compaction and the Size of DNA on the Nuclear Transfer Efficiency after Microinjection in Synchronized Cells.* Pharmaceutics, 2015. **7**(2): p. 64-73.
13. Hou, X., et al., *Lipid nanoparticles for mRNA delivery.* Nat Rev Mater, 2021. **6**(12): p. 1078-1094.
14. Williams, M.C., et al., *Effect of pH on the overstretching transition of double-stranded DNA: evidence of force-induced DNA melting.* Biophys J, 2001. **80**(2): p. 874-81.
15. Every, A.E. and I.M. Russu, *Influence of magnesium ions on spontaneous opening of DNA base pairs.* J Phys Chem B, 2008. **112**(25): p. 7689-95.
16. Sissi, C. and M. Palumbo, *Effects of magnesium and related divalent metal ions in topoisomerase structure and function.* Nucleic Acids Res, 2009. **37**(3): p. 702-11.
17. Cheng, Q., et al., *Selective organ targeting (SORT) nanoparticles for tissue-specific mRNA delivery and CRISPR-Cas gene editing.* Nat Nanotechnol, 2020. **15**(4): p. 313-320.
18. Omo-Lamai, S., et al., *Physicochemical Targeting of Lipid Nanoparticles to the Lungs Induces Clotting: Mechanisms and Solutions.* Adv Mater, 2024. **36**(26): p. e2312026.
19. Vaidya, A., et al., *Analytical Characterization of Heterogeneities in mRNA-Lipid Nanoparticles Using Sucrose Density Gradient Ultracentrifugation.* Anal Chem, 2024. **96**(14): p. 5570-5579.

20. Li, S., et al., *Payload distribution and capacity of mRNA lipid nanoparticles.* Nat Commun, 2022. **13**(1): p. 5561.
21. Omo-Lamai, S., et al., *Lipid Nanoparticle-Associated Inflammation is Triggered by Sensing of Endosomal Damage: Engineering Endosomal Escape Without Side Effects.* bioRxiv, 2024.
22. Simonsen, J.B., *A perspective on bleb and empty LNP structures.* Journal of Controlled Release, 2024. **373**: p. 952-961.
23. Caselli, L., et al., *Small-angle X-ray and neutron scattering applied to lipid-based nanoparticles: Recent advancements across different length scales.* Adv Colloid Interface Sci, 2024. **327**: p. 103156.
24. Hammel, M., et al., *Correlating the Structure and Gene Silencing Activity of Oligonucleotide-Loaded Lipid Nanoparticles Using Small-Angle X-ray Scattering.* ACS Nano, 2023. **17**(12): p. 11454-11465.
25. Gilleron, J., et al., *Image-based analysis of lipid nanoparticle-mediated siRNA delivery, intracellular trafficking and endosomal escape.* Nat Biotechnol, 2013. **31**(7): p. 638-46.
26. Munson, M.J., et al., *A high-throughput Galectin-9 imaging assay for quantifying nanoparticle uptake, endosomal escape and functional RNA delivery.* Commun Biol, 2021. **4**(1): p. 211.
27. Fu, Y., et al., *Inhibition of cGAS-Mediated Interferon Response Facilitates Transgene Expression.* iScience, 2020. **23**(4): p. 101026.
28. Zhang, C., et al., *Structural basis of STING binding with and phosphorylation by TBK1.* Nature, 2019. **567**(7748): p. 394-398.
29. Haag, S.M., et al., *Targeting STING with covalent small-molecule inhibitors.* Nature, 2018. **559**(7713): p. 269-273.
30. Sussman, C., R.A. Liberatore, and M.M. Drozdz, *Delivery of DNA-Based Therapeutics for Treatment of Chronic Diseases.* Pharmaceutics, 2024. **16**(4).
31. Hardee, C.L., et al., *Advances in Non-Viral DNA Vectors for Gene Therapy.* Genes (Basel), 2017. **8**(2).
32. Li, A., et al., *A Self-Deleting AAV-CRISPR System for In Vivo Genome Editing.* Mol Ther Methods Clin Dev, 2019. **12**: p. 111-122.
33. Rowland, S., et al., *Layer-by-Layer Nanoparticle Assembly for Biomedicine: Mechanisms, Technologies, and Advancement via Acoustofluidics.* ACS Appl Nano Mater, 2024. **7**(14): p. 15874-15902.
34. Shepherd, S.J., et al., *Scalable mRNA and siRNA Lipid Nanoparticle Production Using a Parallelized Microfluidic Device.* Nano Lett, 2021. **21**(13): p. 5671-5680.
35. Shepherd, S.J., et al., *Throughput-scalable manufacturing of SARS-CoV-2 mRNA lipid nanoparticle vaccines.* Proc Natl Acad Sci U S A, 2023. **120**(33): p. e2303567120.
36. Subraveti, S.N., et al., *Synthesizing Lipid Nanoparticles by Turbulent Flow in Confined Impinging Jet Mixers.* J Vis Exp, 2024(210).
37. Yang, L., et al., *Solution scattering at the Life Science X-ray Scattering (LiX) beamline.* J Synchrotron Radiat, 2020. **27**(Pt 3): p. 804-812.
38. Hopkins, J.B., R.E. Gillilan, and S. Skou, *BioXTAS RAW: improvements to a free open-source program for small-angle X-ray scattering data reduction and analysis.* J Appl Crystallogr, 2017. **50**(Pt 5): p. 1545-1553.
39. Meisburger, S.P., D. Xu, and N. Ando, *REGALS: a general method to deconvolve X-ray scattering data from evolving mixtures.* IUCrJ, 2021. **8**(Pt 2): p. 225-237.
40. Grant, T., *Describing small-angle scattering profiles by a limited set of intensities.* Journal of Applied Crystallography, 2022. **55**(5): p. 1116-1124.
41. Whitten, A.E., S.Z. Cai, and J. Trewhella, *:: modules for the analysis of small-angle neutron contrast variation data from biomolecular assemblies.* Journal of Applied Crystallography, 2008. **41**: p. 222-226.

42. Grant, T.D., *Ab initio electron density determination directly from solution scattering data.* Nature Methods, 2018. **15**(3): p. 191-193.

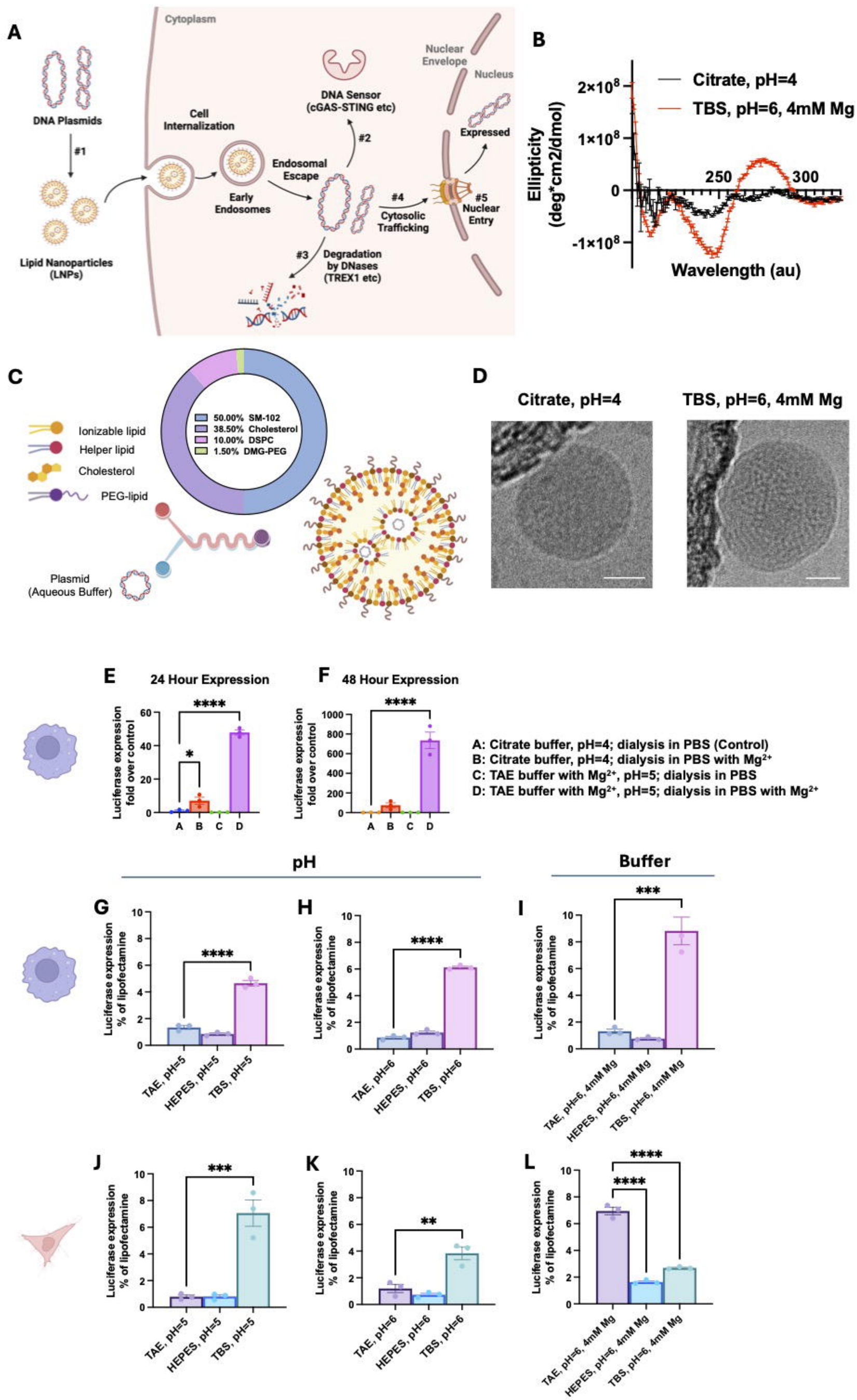
A
Cytoplasm
DNA Plasmids
#1
Lipid Nanoparticles (LNPs)
Cell Internalization
Early Endosomes
Endosomal Escape
DNA Sensor (cGAS-STING etc)
#2
#3
Degradation by DNases (TREX1 etc)
#4
Cytosolic Trafficking
Nuclear Envelope
Nucleus
#5 Nuclear Entry
Expressed
B
Citrate, pH=4
TBS, pH=6, 4mM Mg
Ellipticity (deg*cm2/dmol)
Wavelength (au)
C
50.00% SM-102
38.50% Cholesterol
10.00% DSPC
1.50% DMG-PEG
Ionizable lipid
Helper lipid
Cholesterol
PEG-lipid
Plasmid (Aqueous Buffer)
D
Citrate, pH=4
TBS, pH=6, 4mM Mg
E
24 Hour Expression
F
48 Hour Expression
Luciferase expression fold over control
A: Citrate buffer, pH=4; dialysis in PBS (Control)
B: Citrate buffer, pH=4; dialysis in PBS with Mg2+
C: TAE buffer with Mg2+, pH=5; dialysis in PBS
D: TAE buffer with Mg2+, pH=5; dialysis in PBS with Mg2+
pH
Buffer
G
H
I
J
K
L
Luciferase expression % of lipofectamine
TAE, pH=5
HEPES, pH=5
TBS, pH=5
TAE, pH=6
HEPES, pH=6
TBS, pH=6
TAE, pH=6, 4mM Mg
HEPES, pH=6, 4mM Mg
TBS, pH=6, 4mM Mg

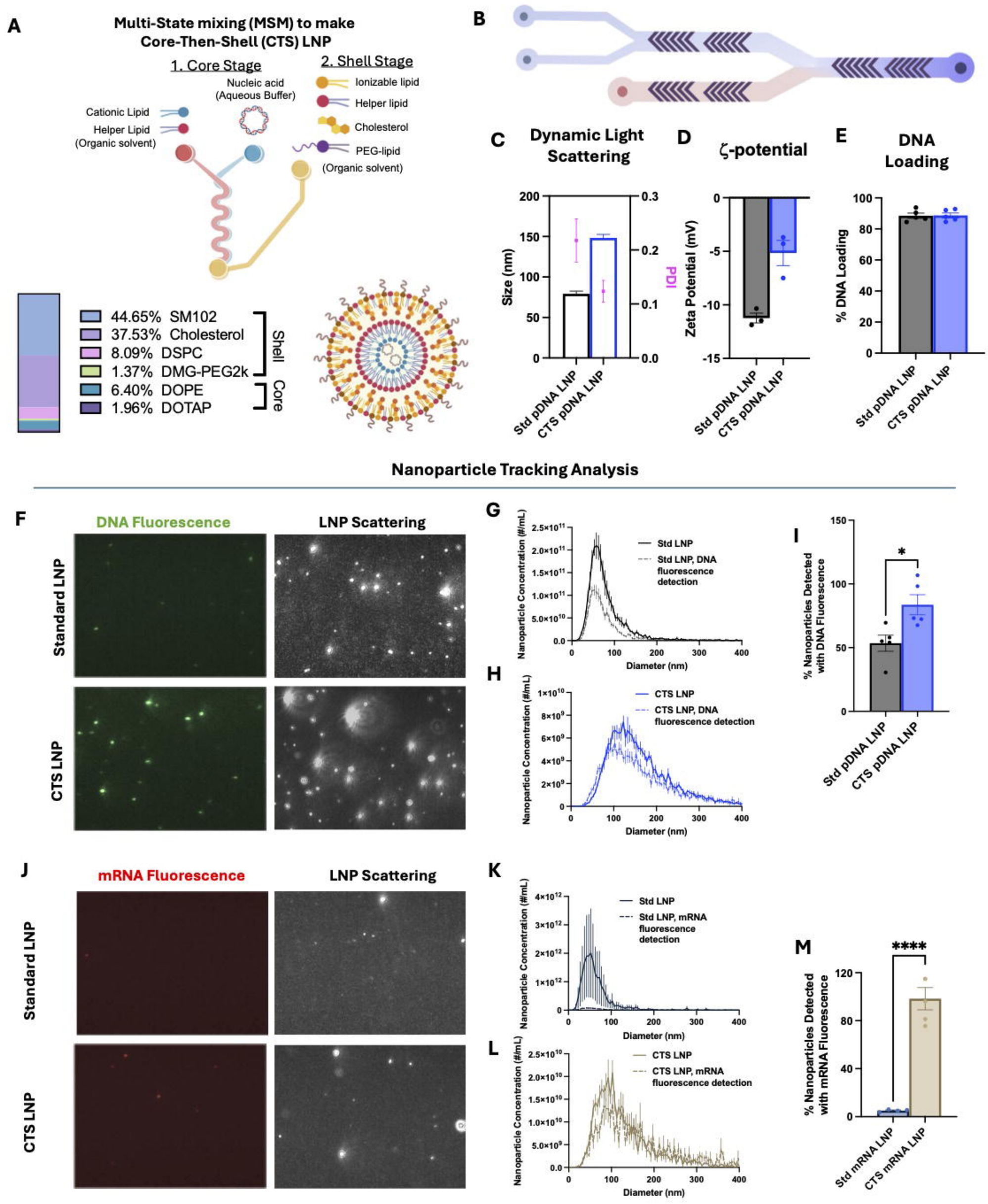
A
Multi-State mixing (MSM) to make Core-Then-Shell (CTS) LNP
1. Core Stage
2. Shell Stage
Nucleic acid (Aqueous Buffer)
Cationic Lipid
Helper Lipid (Organic solvent)
Ionizable lipid
Helper lipid
Cholesterol
PEG-lipid (Organic solvent)
44.65% SM102
37.53% Cholesterol
8.09% DSPC
1.37% DMG-PEG2k
6.40% DOPE
1.96% DOTAP
Shell
Core
B
C
Dynamic Light Scattering
Size (nm)
PDI
Std pDNA LNP
CTS pDNA LNP
D
ζ-potential
Zeta Potential (mV)
E
DNA Loading
% DNA Loading
Nanoparticle Tracking Analysis
F
DNA Fluorescence
LNP Scattering
Standard LNP
CTS LNP
G
Std LNP
Std LNP, DNA fluorescence detection
Nanoparticle Concentration (#/mL)
Diameter (nm)
H
CTS LNP
CTS LNP, DNA fluorescence detection
I
% Nanoparticles Detected with DNA Fluorescence
J
mRNA Fluorescence
LNP Scattering
K
Std LNP
Std LNP, mRNA fluorescence detection
L
CTS LNP
CTS LNP, mRNA fluorescence detection
M
% Nanoparticles Detected with mRNA Fluorescence
Std mRNA LNP
CTS mRNA LNP

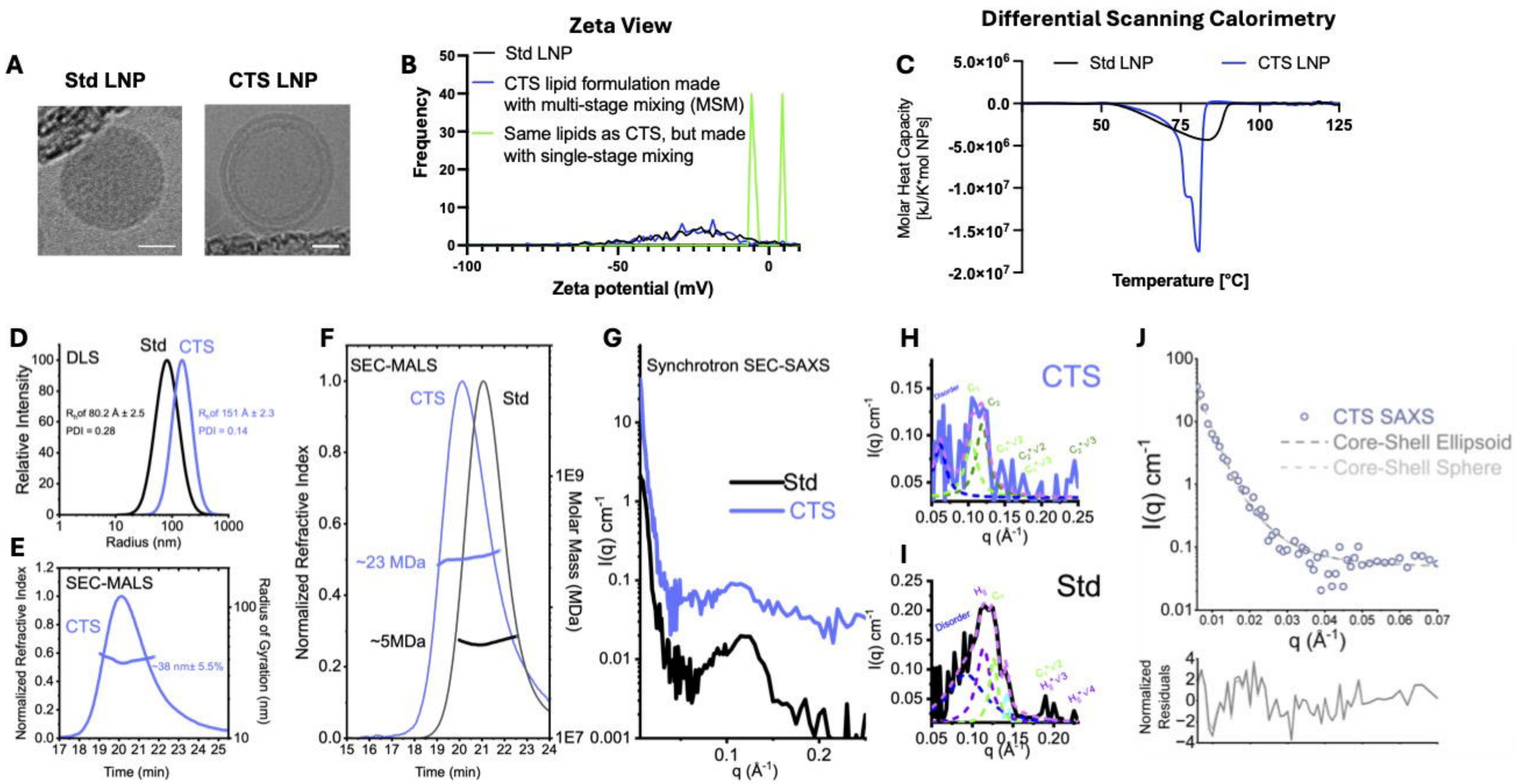
A
Std LNP
CTS LNP
B
Zeta View
Std LNP
CTS lipid formulation made with multi-stage mixing (MSM)
Same lipids as CTS, but made with single-stage mixing
Frequency
Zeta potential (mV)
C
Differential Scanning Calorimetry
Std LNP
CTS LNP
Molar Heat Capacity [kJ/K*mol NPs]
Temperature [°C]
D
DLS
Std
CTS
Relative Intensity
Radius (nm)
E
SEC-MALS
CTS
~38 nm± 5.5%
Normalized Refractive Index
Radius of Gyration (nm)
Time (min)
F
SEC-MALS
CTS
Std
~23 MDa
~5MDa
Normalized Refractive Index
Molar Mass (MDa)
Time (min)
G
Synchrotron SEC-SAXS
Std
CTS
I(q) cm⁻¹
q (Å⁻¹)
H
CTS
I(q) cm⁻¹
q (Å⁻¹)
I
Std
I(q) cm⁻¹
q (Å⁻¹)
J
CTS SAXS
Core-Shell Ellipsoid
Core-Shell Sphere
I(q) cm⁻¹
q (Å⁻¹)
Normalized Residuals

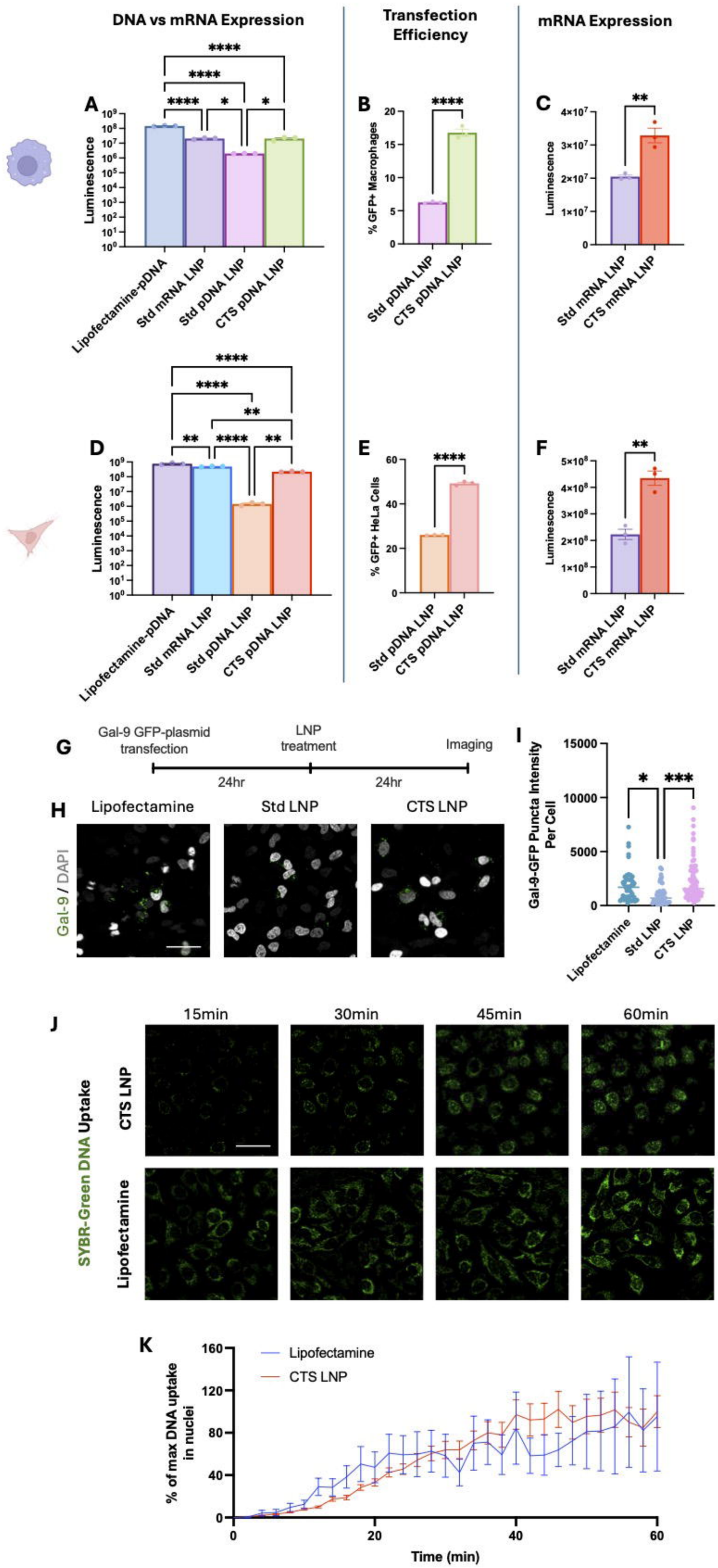
DNA vs mRNA Expression
Transfection Efficiency
mRNA Expression
A
B
C
D
E
F
Luminescence
% GFP+ Macrophages
% GFP+ HeLa Cells
Lipofectamine-pDNA
Std mRNA LNP
Std pDNA LNP
CTS pDNA LNP
CTS mRNA LNP
G
Gal-9 GFP-plasmid transfection
LNP treatment
Imaging
24hr
24hr
H
Lipofectamine
Std LNP
CTS LNP
Gal-9 / DAPI
I
Gal-9-GFP Puncta Intensity Per Cell
J
15min
30min
45min
60min
CTS LNP
Lipofectamine
SYBR-Green DNA Uptake
K
Lipofectamine
CTS LNP
% of max DNA uptake in nuclei
Time (min)

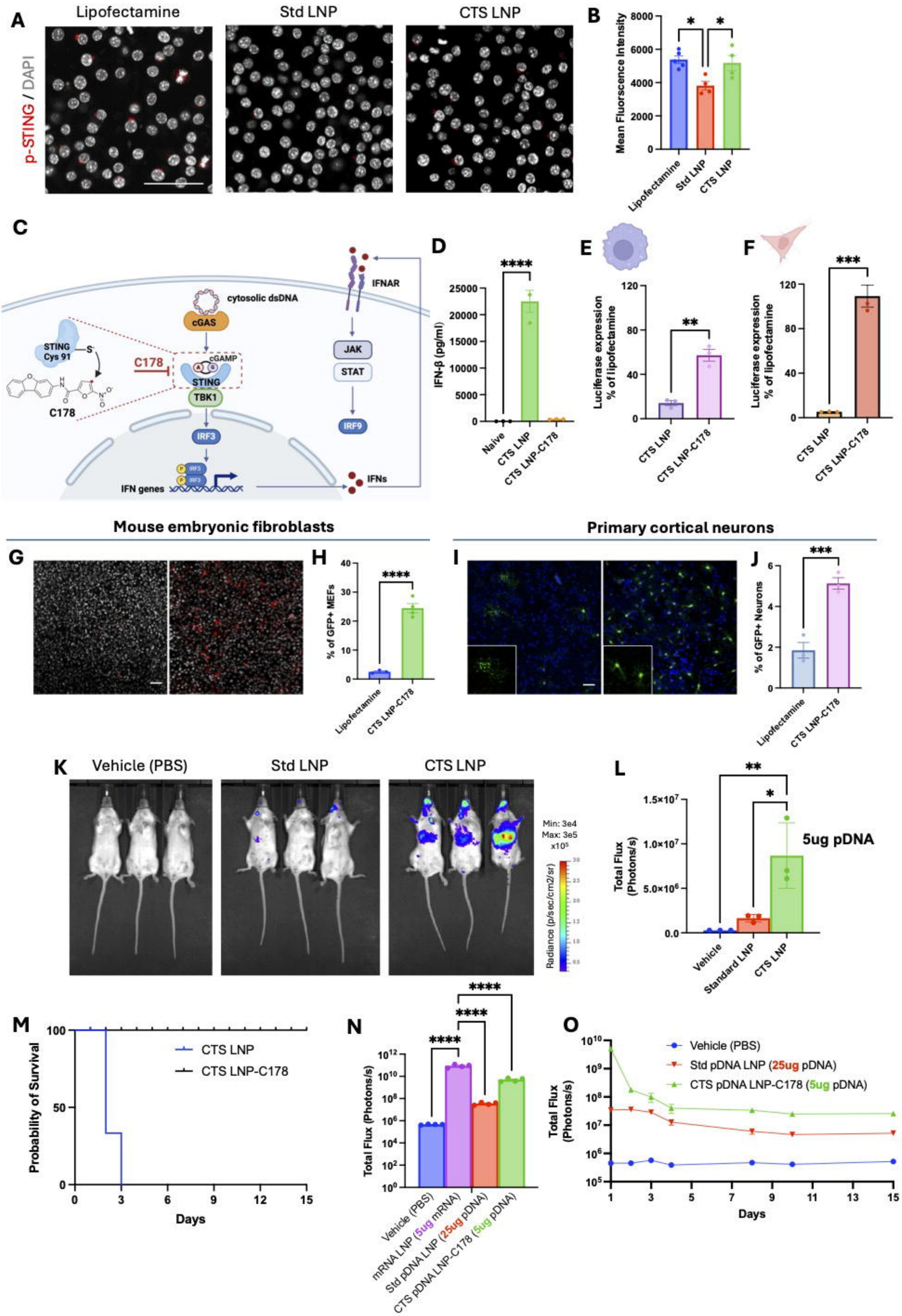
A
Lipofectamine
Std LNP
CTS LNP
p-STING / DAPI
B
Mean Fluorscence Intensity
Lipofectamine
Std LNP
CTS LNP
C
cytosolic dsDNA
cGAS
cGAMP
STING
TBK1
IRF3
IFN genes
IFNs
IFNAR
JAK
STAT
IRF9
STING Cys 91
C178
D
IFN-β (pg/ml)
Naive
CTS LNP
CTS LNP-C178
E
Luciferase expression % of lipofectamine
CTS LNP
CTS LNP-C178
F
Luciferase expression % of lipofectamine
CTS LNP
CTS LNP-C178
Mouse embryonic fibroblasts
G
H
% of GFP+ MEFs
Lipofectamine
CTS LNP-C178
Primary cortical neurons
I
J
% of GFP+ Neurons
Lipofectamine
CTS LNP-C178
K
Vehicle (PBS)
Std LNP
CTS LNP
Min: 3e4
Max: 3e5
Radiance (p/sec/cm2/sr)
L
Total Flux (Photons/s)
5ug pDNA
Vehicle
Standard LNP
CTS LNP
M
Probability of Survival
CTS LNP
CTS LNP-C178
Days
N
Total Flux (Photons/s)
Vehicle (PBS)
mRNA LNP (5ug mRNA)
Std pDNA LNP (25ug pDNA)
CTS pDNA LNP-C178 (5ug pDNA)
O
Total Flux (Photons/s)
Vehicle (PBS)
Std pDNA LNP (25ug pDNA)
CTS pDNA LNP-C178 (5ug pDNA)
Days